Post-mitotic myotubes repurpose the cytokinesis machinery to effect cellular guidance

Shuo Yang[1], Jennifer McAdow[1], Yingqiu Du[1], Jennifer Trigg[2], Paul H. Taghert[2], and Aaron N. Johnson[1,3]

[1]Department of Developmental Biology
[2]Department of Neuroscience
Washington University School of Medicine
St. Louis, MO 63110

[3]Author for correspondence: anjohnson@wustl.edu

Running Title: Bsd activates Polo during myogenesis

Summary

Myotube guidance is an essential step of muscle development that ultimately establishes the final musculoskeletal pattern, yet the mechanisms that guide post-mitotic myotubes to the correct skeletal attachment sites are poorly understood. Here, we describe a novel myogenic pathway that is regulated by the previously uncharacterized Vaccinia Related Kinase (VRK) family member Back Seat Driver (Bsd). Bsd modulates microtubule dynamics to direct myotube guidance in *Drosophila* embryos, and preserves cellular identity by preventing myotube-myotube fusion. Mechanistically, Bsd activates Polo kinase in nascent myotubes to regulate cellular guidance. Tumbleweed (Tum) is an essential Polo effector during cytokinesis, and we show Tum performs a critical role in attachment site selection. We also found that the mammalian Bsd orthologue Vrk3 is required for myotube morphogenesis, and that Vrk3 activates the Polo orthologue Plk1. Our studies have uncovered a conserved pathway in which Bsd activates the cytokinesis machinery in post-mitotic cells to direct myotube guidance.

Introduction

Dynamic changes to cytoskeletal architecture drive an extensive array of cellular processes including morphogenesis, migration, fusion, and cell division. Polo-like kinases (Plks) direct a variety of cytoskeletal-based processes during both mitosis and meiosis that include centriole maturation, aster assembly, chromosome segregation, and the initiation of cytokinesis (Cabral et al., 2019; Lane and Nigg, 1996; Lénárt et al., 2007; Liu et al., 2012; Liu and Erikson, 2002). The *Drosophila* genome encodes two Plks, Polo kinase (Polo) and Sak kinase, and Polo is often referred to as the master regulator of mitosis due to its numerous functions during cell division (Carmena et al., 2012). The microtubule cytoskeleton serves as both a target and a regulator of Polo activity. During interphase, Polo is recruited to centrioles where it is essential for centriole maturation, and for the assembly of the pericentriolar material that ultimately generate functional centrosomes capable of microtubule spindle assembly and faithful chromosome segregation (Donaldson et al., 2001; Fu and Lipinszki, 2016; Novak et al., 2016). Following chromosome segregation, Polo directs the localization of two effector proteins, the GTPase activating protein Tumbleweed (Tum) and the kinesin microtubule motor protein Pavarotti (Pav), to the cytokinesis initiation complex where Tum and Pav bind cortical microtubules and position the contractile ring during furrow formation (Adams et al., 1998; Carmena et al., 1998; Ebrahimi et al., 2010). Microtubules also serve as a scaffold to sequester Polo, and inhibit Polo catalytic activity during key stages of mitosis and meiosis (Archambault et al., 2008; Bonner et al., 2020). Despite our extensive understanding of how Polo organizes the microtubule cytoskeleton during cell division, a role for Polo in post-mitotic cells has not been described. In addition, the mechanisms that regulate Polo activation are incompletely understood**.**

Cellular guidance, which is distinct from cell migration, is a cytoskeleton-dependent morphogenetic process in which the cell remains spatially fixed, and generates projections that interact with or connect to other cells. Axon guidance is perhaps the most studied form of cellular guidance and provides the foundation for connecting neurons throughout the nervous system (McCormick and Gupton, 2020). Vascular tip cells also undergo cellular guidance and send long projections to connect with distant tips cells, and the resulting cellular bridge forms a new lumen that subsequently becomes a blood-carrying vessel (Adams and Eichmann, 2010). In insects, terminal cells are specialized tracheal tip cells that extend long terminal branches, which eventually cover target tissues for gas exchange (Best, 2019). Nascent myotubes also undergo cellular guidance, and extend bipolar projections that connect with tendon precursors and in turn to the skeleton (Schnorrer and Dickson, 2004). Similar to vascular tip cells, myotube

guidance plays a key role in tissue patterning as defects in myotube guidance disrupt the overall configuration of the musculoskeletal system (Yang et al., 2020). The embryonic body wall musculature in *Drosophila*, which is analogous to vertebrate skeletal muscle, has served as the main model to identify the molecular regulators of myotube guidance. Although a number of extracellular signaling pathways and intracellular cytoskeletal regulatory proteins have been identified (Guerin and Kramer, 2009b; Johnson et al., 2013; Kramer et al., 2001; Schnorrer et al., 2007; Yang et al., 2020), a holistic understanding of myotube guidance in insects, much less in vertebrates, remains far from complete.

In a forward genetic screen, we identified the serine/threonine (ser/thr) kinase Back seat driver (Bsd) as a novel regulator of the microtubule cytoskeleton during myotube guidance. Using affinity-purification and mass spectrometry (AP-MS), we found that Bsd physically interacts with Polo. Subsequent genetic and biochemical studies showed that Bsd activates Polo both *in vitro* and *in vivo*, and that Bsd acts upstream of Polo during myotube guidance. Tum and Pav are downstream effectors of Polo during cytokinesis, and are also required for microtubule reorganization during muscle morphogenesis. Tum directs both myotube elongation and muscle attachment site selection, which are the hallmarks of myotube guidance. Furthermore, inhibiting the Bsd orthologue Vrk3 or the Polo orthologue Plk1 in cultured mouse myoblasts disrupted myotube elongation, and we found that Vrk3 is a potent activator of Plk1. We have thus uncovered a conserved myogenic pathway in which Bsd activates the Polo-Tum-Pav cytokinesis machinery in post-mitotic myotubes to regulate the microtubule cytoskeleton during myotube guidance, and to correctly pattern the musculoskeletal system.

Results

To identify novel regulators of muscle morphogenesis, we performed an EMS-based forward genetic screen (Fig. 1A) and identified a strong allele, that we named *back seat driver (bsd)*, which disrupted overall body wall muscle patterning (Fig. 1B). A number of *bsd* muscles showed elongation and attachment site phenotypes (Fig. 1B,C), indicative of myotube guidance defects (Williams et al., 2015; Yang et al., 2020). RNA deep sequencing (RNA-seq) of *bsd* embryos identified 10 potentially damaging coding region variants, including a nonsense mutation (Q545*) in *CG8878* (Fig.1D). Two overlapping deficiencies [*Df(2R)BSC199* and *Df(2R)BSC699*] that uncover *CG8878* failed to complement the *bsd* allele (Fig. S1A), and two large genomic constructs that encode *CG8878* fully rescued the *bsd* myogenic phenotype (Fig. 1B-D). To further validate our genetic mapping, we outcrossed the Q545* allele away from the genomic rescue constructs, and found that the *bsd* phenotype faithfully segregated with the *CG8878* nonsense mutation (Fig. 1B,C). Since the Q545* allele presumably caused navigational defects during myotube guidance, we named *CG8878 back seat driver*.

Bsd is a member of the VRK family of proteins

Bsd encodes a conserved serine/threonine (ser/thr) kinase, and has one *Drosophila* paralog, Ballchen (Ball; Fig. S1B). Bsd and Ball are orthologues of the Vaccinia Related Kinases (VRK), but a role for VRK family proteins in myogenesis have not previously been reported. The VRK proteins each contain a single conserved kinase domain (KD) near the N-terminus, and a highly variable C-terminus (Fig. S1C). Bsd is most similar to VRK3 (Fig. S1B), but is unique among the VRK proteins in that a linker region splits the kinase domain (Fig. S1C). The nonsense mutation we recovered in our genetic screen (hereafter bsd^{1}) truncates the Bsd KD and removes the variable C-terminus, but does not alter the linker region or the ATP binding pocket (Fig. 1D).

The Bsd paralog Ball is required to maintain both germ line and neuronal stem cell populations in *Drosophila* (Herzig et al., 2014; Yakulov et al., 2014), and mice with gene traps in *Vrk1* showed defects in germ line stem cell maintenance but no other obvious phenotypes (Schober et al., 2011; Wiebe et al., 2010). Several substrates of VRK family proteins have been identified including p53, c-Jun, and Barrier to Autointegration Factor (BAF), which argues the VRK proteins play important roles in cell division and nuclear envelope architecture (Nichols et al., 2006; Sevilla et al., 2004; Vega et al., 2004). In addition, pathogenic VRK1 variants have been identified in patients with motor neuropathies, which may arise from defects in neurite outgrowth (El-Bazzal et al., 2019; Greenbaum et al., 2020; Martín-Doncel and Rojas, 2019;

Renbaum et al., 2009; Stoll et al., 2016). Although a number of essential and clinically relevant roles for the VRK proteins are emerging, comparatively little is known about the molecular and biological functions of the VRK3 subfamily.

Bsd directs myotube guidance

We used our previously established guidance assays to fully characterize the role of *bsd* during myogenesis (Yang et al., 2020). An embryonic segment will develop thirty distinct muscles, each of which is derived from a single founder cell. Each founder cell will fuse with neighboring fusion competent myoblasts to form a syncytial muscle, as well as elongate and identify a stereotypic muscle attachment site at the segment border. Within a given segment, each founder cell expresses a distinct combination of transcription factors such that each muscle has a unique identity. *5053.Gal4* is active in the Ventral Longitudinal 1 (VL1) muscles and the VL1 founder cells were correctly specified in Stage 12 bsd^1 embryos (Fig. S1D). *slou.Gal4* is highly active in the Longitudinal Oblique 1 (LO1) muscles, as well as in the Dorsal Transverse 1 (DT1) and Ventral Transverse 1 (VT1) muscles, and the number of *slou.Gal4* positive cells was not significantly different between wild-type and bsd^1 Stage 12 embryos (Fig. S1E). These data strongly suggest that Bsd does not regulate VL1, LO1, DT1, or VT1 founder cell specification.

VL1, LO1, DT1, and VT1 myotubes acquire unique yet stereotypic morphologies by Stage 16 due to myotube elongation and attachment site selection (Fig. 1E,F). We define myotube guidance as the process in which a nascent myotube both elongates and identifies the correct muscle attachment site. In Stage 16 bsd^1 embryos the VL1, LO1, DT1, and VT1 myotubes showed elongation and attachment site defects (Fig. 1E-H), which is consistent with a role for Bsd in regulating myotube guidance. We live imaged LO1 myotubes that expressed a cytoplasmic GFP and nuclear RFP under the control of *slou.Gal4*. Control LO1 myotubes underwent a highly regulated dorsal elongation followed by a sharp anterior turn that ultimately resulted in an oblique muscle morphology [Movie 1, (Yang et al., 2020)]. In contrast, bsd^1 LO1 myotubes often failed turn to the anterior, which resulted in a transverse morphology (Movie 1). Bsd is thus an essential regulator of myotube guidance.

Interestingly, bsd^1 LO1 myotubes also fused other elongated *slou.gal4* positive myotubes at low frequencies (27.1%, n=48, Movie 2). We used a similar assay to visualize guidance defects in *heartless* (*htl)* LO1 myotubes and, even though *htl* myotubes mislocalized in a manner similar to bsd^1 myotubes, we did not observe myotube-myotube fusion in *htl* mutants (Yang et al., 2020). These studies argue that myotube-myotube fusion in bsd^1 embryos is not

due to the mislocalization of mutant myotubes, but is likely due to an intrinsic property that allows *bsd*^{1} myotubes to fuse. Since each myotube is derived from a unique founder cell, our live imaging results show that Bsd maintains cellular identity during muscle morphogenesis.

We next asked if Bsd regulates fusion between founder cells and fusion competent myoblasts. The standardized fusion assay uses *rp298.nlacZ* to visualize myonuclei in founder cells and nascent myotubes; the number of *rp298.nlacZ* positive myonuclei will increase over developmental time as the founder cells fuse with fusion competent myoblasts. At Stage 12, when the first events of myoblast fusion have completed, we observed a modest yet significant decrease in the *bsd*^{1} fusion index compared to controls (85.4%, n=60 segments, Fig. 1I). This trend continued through Stage 14 (78.0%, n=60, Fig. 1I) and Stage 16 (72.7%, n=60, Fig. 1I). Although Bsd plays a role in both canonical myoblast fusion and myotube-myotube fusion, the frequency of fusion defects in *bsd*^{1} embryos was far less than the frequency of myotube guidance defects. These observations suggest that Bsd regulates myoblast fusion and myotube guidance through independent mechanisms.

Bsd functions in the mesoderm to direct myotube guidance

To understand if Bsd functions in the mesoderm to regulate myotube guidance, we expressed wild-type Bsd in *bsd*^{1} embryos using the pan-mesodermal driver *24B.Gal4*. Control *bsd*^{1}*/Df(2R)BSC199* embryos showed dramatic muscle patterning defects, and these myogenic defects were suppressed in *bsd*^{1}*/Df(2R)BSC199* embryos that expressed Bsd in the mesoderm (Fig. 2A). Proteins in the VRK family contain a highly conserved ATP binding pocket that is essential for kinase catalytic activity [(Fig. S1C), (Shin et al., 2011)]. Computational structural models predicted that Bsd isoleucine 129 binds ATP (Fig. 2A), and we found that Bsd.I129A was unable to suppress the *bsd*^{1}*/Df(2R)BSC199* phenotype (Fig. 2A). These genetic rescue experiments argue that Bsd kinase activity in the mesoderm is required for proper muscle morphogenesis.

We generated and validated an antibody against Bsd to characterize its subcellular localization during myogenesis (Fig. S2A-C). Immunohistochemistry showed that Bsd localizes to both the cytoplasm and the nucleus in the somatic mesoderm (Fig. 2B). Interestingly, Bsd showed a progressive nuclear enrichment during myogenesis (Fig. 2B), in which the relative level of Bsd in myonuclei was significantly less than that of neighboring Mef2-negative cells at the initiation of myotube elongation (Stage 11, 76.7%, n=215, Fig. S2D). However, once myotube elongation initiated, the relative level of Bsd in myonuclei was significantly greater than that of Mef2-negative cells (Stage 12, 119.0%, n=500, Fig. S2D), and this nuclear enrichment

continued through muscle attachment site selection (Stage 14, 134.9%, n=286, Fig. S2D). After myotube guidance was complete (Stage 16), Bsd was evenly distributed between the cytoplasm and the myonuclei (Fig. 2B). The dynamic localization of Bsd suggests that Bsd shuttles between the cytoplasm and the nucleus during myogenesis, and that Bsd nuclear localization peaks during myotube guidance**.**

Bsd regulates the microtubule cytoskeleton during myotube guidance

Myotube guidance is accomplished through dynamic changes in both the actin and microtubule cytoskeletons (Guerin and Kramer, 2009a, b; Yang et al., 2020). To investigate the role of Bsd in regulating cytoskeletal dynamics, we live imaged LO1 myotubes that expressed F-actin localized LifeAct.RFP and microtubule minus-end localized Nod.GFP under the control of *slou.Gal4*. The microtubule cytoskeleton is cortical in nascent myotubes, and as the myotube breaks symmetry and begins to elongate, the microtubules reorganize to form linear arrays (Guerin and Kramer, 2009b). In wild-type LO1 myotubes, *slou.Gal4* driven Nod.GFP fluorescence was first detected at Stage 12, when the microtubule cytoskeleton had begun to reorganize (Fig. 3A,B; Movie 3). Nod.GFP-labeled microtubule minus-end arrays remained linear throughout myotube guidance, and did not overlap with F-actin at the myotube leading edges. Microtubule reorganization was delayed by over 60min in bsd^1 myotubes, and the microtubule minus-ends often accumulated in the F-actin domain at the leading edge (Fig. 3A,B, Movie 3). Importantly, the absolute levels of F-actin were comparable between control and bsd^1 myotubes (Fig. 3B). These live imaging results suggest that Bsd predominantly regulates the microtubule cytoskeleton.

In addition to delayed reorganization of the microtubule cytoskeletal, some bsd^1 myotubes oscillated between linear and cortical microtubule arrays. We measured the shape of the Nod.GFP domain at each time point of our live imaging experiments, and found that Nod.GFP remained consistently linear in wild-type LO1 myotubes (Fig. 3C), as evidenced by a low average ‘roundness’ score (0.28, n=162). However, bsd^1 LO1 myotubes showed a broad range of roundness scores (0.22-0.97, n=162) that were due to dramatic fluctuations in the shape of the Nod.GFP domain (Fig. 3C). On average, the Nod.GFP domain was more round in bsd^1 LO1 myotubes than controls (0.56), suggesting that Bsd is required to initiate microtubule reorganization during myotube elongation, and to maintain the linear arrays of microtubules during myotube guidance.

The muscle attachment angle for LO1 myotubes ranges between 120-150° in wild-type embryos, and is consistent with an oblique morphology (Yang et al., 2020). The angle of the

linear Nod.GFP domain in wild-type LO1 myotubes remained constant throughout myotube guidance (Fig. 3C), and averaged 129.6°. In *bsd*^{1} myotubes, the angle of the Nod.GFP domain was highly variable and averaged 93.2°, which is consistent with a transverse morphology (Fig. 3C). The angle of the microtubule arrays during myotube guidance largely paralleled the axis of elongation, in both control and mutant myotubes, and is thus indicative of final muscle morphology.

Mechanistically, γ-tubulin is an essential minus-end nucleator that initiates the assembly of new microtubules [reviewed in (Tillery et al., 2018)]. Prior to myotube elongation, γ-tubulin foci are predominantly localized to the myotube cortex, and as the microtubule cytoskeleton reorganizes during elongation, γ-tubulin foci appear in the internal cytoplasm and a subset of these internal foci are perinuclear [Figs. 3D, S3A (Guerin and Kramer, 2009b)]. The internal γ-tubulin foci are thought to be sites for *de novo* microtubule assembly that drives myotube elongation. We used myonuclei number as an indicator of myogenic progression in fixed Stage 12 embryos, and found that there were no significant differences in the number of cortical or internal γ-tubulin foci between control (cortical=6.7, internal=1.5, n=8) or *bsd*^{1} (cortical=5.5, internal=2.4, n=11) mononucleate LO1 myotubes (Fig. S3A,B). In multinucleate myotubes, there were significantly fewer internal γ-tubulin foci in *bsd*^{1} mutants (internal=2.6, n=12, Fig. 3D,E) compared to controls (internal=10.2, n=13). However, there was no significant difference in the number of cortical foci in multinucleate LO1 myotubes (control=9.4, *bsd*^{1}=13.9, Fig. 3D,E). Bsd is thus required to establish internal cytoplasmic γ-tubulin foci during microtubule reorganization, suggesting that Bsd regulates myotube guidance by promoting *de novo* microtubule assembly.

Bsd physically interacts with Polo kinase

To understand the molecular pathways by which Bsd regulates myotube guidance, we took an unbiased proteomics approach to identify Bsd interacting proteins. GST-tagged Bsd was purified from bacterial lysates, and used for AP-MS to identify Bsd interacting proteins from 12-24hr embryo lysates (Fig. S4A). The most abundant protein recovered from our AP-MS experiment was Bsd itself, which shows GST-Bsd was successfully immobilized during affinity purification (Fig. 4A). Among the Bsd interacting proteins, microtubule-associated protein 205 (Map205) and Polo are known regulators of the microtubule cytoskeleton, and Jaguar (Jar) is a Myosin VI that binds F-actin. We had previously shown the RNA binding protein Hoip indirectly regulates cytoskeletal dynamics during myotube elongation (Johnson et al., 2013; Williams et al., 2015), and the RNA binding proteins Lost and IGF-II mRNA Binding Protein (Imp) showed potential interactions with Bsd. Surprisingly, our AP-MS only identified one protein with a

potential myogenic function, which was Yolk Protein 3 (Yp3) that directs flight muscle development through an unknown mechanism (Schnorrer et al., 2010). We screened for protein-protein interactions between Bsd and Map205, Polo, Jar, Lost, Imp, and Yp3 using affinity tagged proteins expressed in S2 cells, and found a strong, reproducible interaction between wild-type Bsd and Polo (Fig. 4B,C). However the truncated Bsd.Q545* protein, which is analogous to the *bsd*^{1} allele, did not interact with Polo (Fig. 4B,C). These data strongly suggest that Bsd and Polo are components of a common protein complex, and that Bsd-Polo interactions could be attenuated in *bsd*^{1} mutants.

Polo and Bsd function in a single myogenic pathway

The physical interaction between Bsd and Polo suggested Polo could play an essential role in muscle morphogenesis, but a myogenic function for *polo* had not previously been reported. We found that two hypomorphic alleles of *polo*, *polo*^{1} and *polo*^{KG03033}, caused phenotypes similar to those we observed in *bsd*^{1} embryos (Fig. S4B), including the specific myotube elongation and muscle attachment site selection defects we characterized in VL1, LO1, DT1, and VT1 myotubes (Fig. 4D,E). To understand if Bsd and Polo function in the same myogenic pathway we assayed muscle morphogenesis in *bsd*^{1} *polo*^{1} double mutant embryos, and found that *polo*^{1} did not enhance the penetrance or the expressivity of the *bsd*^{1} myogenic phenotype (Fig. 4F-H). Since *polo*^{1} did not enhance the *bsd*^{1} myogenic phenotype, Bsd and Polo may act in a common pathway during myogenesis.

Bsd activates Polo in cultured cells

Polo is activated by phosphorylation at Thr182**,** as is the Polo orthologue Polo-like kinase 1 (Plk1) at the analogous residue (Thr210) (Carmena et al., 2012; Jang et al., 2002; Kachaner et al., 2017). Our genetic and molecular studies suggested that Bsd Ser/Thr kinase activity could phosphorylate and activate Polo. We were unable to GST purify Polo from bacterial lysates, so we expressed affinity-tagged Polo in S2 cells and found that immunopurified Polo showed significantly higher levels of phosphorylated-Thr (pThr) when co-transfected with Bsd compared to controls (fold change=6.4±0.87, n=3, Figs. 5A, S5A). In contrast, Bsd.I129A failed to induce Polo phosphorylation in our S2 cell assay (Fig. S5B), arguing that Polo phosphorylation is indeed dependent on Bsd kinase activity.

Activated Polo is localized to the nucleus in cultured cells (Kachaner et al., 2017), so we asked if Bsd-induced Polo phosphorylation also regulates Polo subcellular location. Wild-type Polo localized to the nucleus in a subset of transfected S2 cells (49.2%, n=17 imaging fields,

Fig. 5B), and the percentage of cells with nuclear Polo significantly increased in cells co-transfected with Bsd (84.3%, n=16, Fig. 5B). Consistent with previous reports (Kachaner et al., 2017), Polo.T182A, which cannot be activated by phosphorylation, did not localize to S2 cell nuclei (0%, n=13, Fig. 5B). The results from our *in vitro* assays demonstrate that Bsd regulates Polo nuclear localization.

Bsd activates Polo to direct muscle morphogenesis

To understand if Bsd regulates Polo activity during myogenesis, we expressed activated Polo (Polo.T182D) in *bsd*^{1} embryos using the muscle-specific driver *Mef2.Gal4*. Activated Polo dramatically suppressed the *bsd*^{1} myogenic phenotype (Fig. 5C), which suggested that Bsd phosphorylates and activates Polo *in vivo*. We assayed Polo phosphorylation in embryo lysates using a Polo-GFP knock-in allele (Buszczak et al., 2007), and found that *bsd*^{1} embryo lysates had significantly less phosphorylated Polo than control lysates (fold change=0.28±0.03, n=3, Fig. 5D). These data argue that Polo is downstream of Bsd during muscle morphogenesis, and that Bsd is required for Polo phosphorylation *in vivo***.**

We characterized Polo subcellular localization in Stage 12 myotubes using the Polo-GFP knock-in allele. Although Polo was detectable in both the nucleus and cytoplasm of nascent myotubes, we did not observe a quantitative difference in Polo subcellular localization between control and *bsd*^{1} embryos (Fig. S5C). An antibody that recognizes human PLK1 pThr210 also recognizes *Drosophila* Polo pThr182 (Bonner et al., 2020; Carmena et al., 2012), and we used this antibody to characterize Polo activation during myogenesis. In control embryos, the amount of pThr182 Polo (pPolo) significantly increased in post-mitotic Mef2-positive nuclei during Stage 12 (St12 early=14.0 a.u., n=502, St12 late=24.2, n=542), suggesting that Polo is activated during myotube guidance (Figs. 5E,F S5D). However, in *bsd*^{1} embryos, the amount of pPolo in Mef2-positive nuclei remained constant during Stage 12 (St12 early=14.2 a.u., n=267, St12 late=14.4, n=710; Figs. 5E,F). Thus, Bsd activates Polo during myotube guidance.

The Polo effector Tum regulates myotube guidance

During cytokinesis, Polo directs the localization of two effector proteins, the GTPase activating protein Tumbleweed (Tum) and the kinesin microtubule motor protein Pavarotti (Pav), to the cytokinesis initiation complex where Tum and Pav bind cortical microtubules and position the contractile ring during furrow formation (D'Avino et al., 2006; Ebrahimi et al., 2010; Gregory et al., 2008; Somers and Saint, 2003). Tum is also required to reorganize the microtubule

cytoskeleton and direct myotube elongation (Guerin and Kramer, 2009b), but Tum was not previously shown to play a role in attachment site selection. Bsd and Polo direct both myotube elongation and attachment site selection, so if Tum is indeed a Polo effector during myogenesis then Tum should also regulate attachment site selection. We used *5053>GFP* and *slou>GFP* to visualize individual myotube morphology in *tum*^{DH15} embryos, and identified strong attachment site defects in *tum*^{DH15} VL1, LO1, DT1, and VT1 myotubes, as well as elongation defects (Fig. 5G,H). The *tum* phenotype is thus consistent with a model in which Tum acts downstream of Polo to direct myotube guidance.

Tum directly binds Polo and Pav in yeast-2-hybrid assays (Ebrahimi et al., 2010; Somers and Saint, 2003), which suggested that Bsd, Polo, Tum, and Pav could be in a common protein complex. However, we could not detect a physical interaction between Bsd and Pav in S2 cells (Fig. S5E). While these experiments do not exclude Bsd from transiently interacting with Pav, it seems likely that Bsd is not a component of the Polo-Tum-Pav protein complex.

We next considered the possibility that, similar to Bsd, Tum functions to prevent myotube-myotube fusion. Although we live imaged myogenesis in several *tum*^{DH15} embryos, we did not observe any myotube fusion events. Thus, Bsd appears to prevent myotube fusion through a Tum-independent pathway.

The Bsd orthologue Vrk3 is required for myotube elongation

Under culture conditions that promote differentiation, immortalized mouse myoblasts (C2C12 cells) will fuse and form nascent myotubes that extensively elongate. To understand if mammalian Vrks have a similar myogenic function to Bsd, we used small interfering RNAs (siRNAs) to knock down Vrk1, Vrk2, and Vrk3 during C2C12 cell differentiation. C2C12 cells treated with Vrk1 and Vrk2 siRNAs were morphologically similar to control treated cells after 7 days of differentiation (Fig. S6A), but C2C12 cells treated with Vrk3 siRNAs showed reduced elongation (Figs. 6A, S6A). Interestingly, our phylogenetic analysis showed Bsd is more similar to Vrk3 than to Vrk1 or Vrk2 (Fig. S1B), and our myogenic assays functionally confirmed the phylogenetic results. Quantitatively, Vrk3 siRNAs reduced myotube length by 34% on average (control=495.3µm, n=230, Vrk3= 325.4µm, n=230, Fig. 6B). Cells treated with control siRNAs showed a largely normal distribution of myotube lengths, while the distribution of Vrk3 treated cells skewed significantly toward shorter myotubes (Fig. 6C). Moreover, the roundness score of Vrk3 knock down myotubes was significantly higher than controls (control=0.15, n=799, Vrk3=0.41, n=1209, Fig. 6D), and Vrk3 knock down cells showed less myoblast fusion than

controls (control fusion index=71.8, n=10 fields, Vrk3=64.2, n=10, Fig. 6E). These results are consistent with a role of Vrk3 in regulating myotube elongation and myoblast fusion.

To understand if the molecular function of Vrk3 is conserved, we performed immunoprecipitation assays in HEK293 cells, and found Vrk3 and Plk1 physically interacted (Fig. 6F). Moreover, Vrk3 promoted Plk1 Thr210 phosphorylation (Fig. 6G). Plk1 was recently shown to regulate myoblast proliferation (Jia et al., 2019); to understand if Plk1 also regulates myotube elongation we treated fully confluent C2C12 myoblasts with the Plk1 inhibitor Volasterib under differentiation conditions. Compared to control treatments, Volasterib reduced myotube length by 53.9% (DMSO=512.4µm, n=230, Volasterib=235.9µm, n=462, Fig. 6B,C). In addition, the roundness score of Volasterib treated myotubes was significantly higher than controls (DMSO=0.158, n=654, Volasterib=0.350, n=657, Fig. 6D). However, Volasterib treatment did not disrupt myoblast fusion (DMSO fusion index=73.3, n=10 fields, Volasterib=77.2, n=10, Fig. 6E). Vrk3 and Plk1 are thus conserved regulators of myotube elongation, and Vrk3 regulates Plk1 activation in mammalian cells.

Discussion

This study has identified a novel pathway in which Bsd acts upstream of Polo to direct cytoskeletal remodeling during myotube guidance. In the absence of Bsd, foci of the microtubule minus-end nucleator γ-tubulin remained cortical in nascent myotubes, and the formation of linear microtubule arrays was delayed. Mechanistically, Bsd activates Polo by promoting $Polo^{T182}$ phosphorylation, and Vrk3 promoted the analogous phosphorylation of Plk1 ($Plk1^{T210}$). Since phosphomimetic $Polo^{T182D}$ largely rescued the myogenic defects in *bsd*^{1} embryos, Bsd-mediated Polo activation is essential for myotube guidance and muscle patterning. We also uncovered a role for Bsd preventing myotube-myotube fusion and maintaining muscle cell identity, which appears to be a Polo-independent function for Bsd.

Polo activation

Bsd localization is dynamic during myogenesis. After founder cell specification, Bsd is diffusely localized in myoblasts, and as myotube guidance initiates Bsd becomes enriched in myonuclei (Fig. 2A). Activated Polo ($Polo^{pT182}$) was enriched in myonuclei only after myotube guidance initiated, and Polo nuclear translocation required Bsd (Fig. 5E, S5D). When Polo is inactive, the C-terminal Polo Box Domain (PBD) binds the kinase domain (KD) and masks a nuclear localization signal (NLS). Activating phosphorylation at T182 exposes the NLS and $Polo^{pT182}$ translocates to the nucleus (Kachaner et al., 2017), which argues that Polo activation occurs in the cytoplasm. Cytoplasmic Bsd most likely activates Polo prior to myotube elongation, and both proteins then accumulate in myonuclei (Fig. 6H).

Polo subcellular localization is also mediated by the microtubule binding proteins Map205 and Matrimony [Matr, (Archambault et al., 2008; Bonner et al., 2020)]. Prior to mitotic entry, Map205 binds the Polo PBD and sequesters Polo in the cytoplasm; as mitosis initiates Cdk-mediated Map205 phosphorylation releases Polo from microtubules to allow for centrosome assembly (Archambault et al., 2008). Mtrm is thought to act through a similar mechanism during meiosis to regulate the available pool of activated Polo (Bonner et al., 2020). Although our data shows that Bsd activates Polo, we cannot exclude the possibility that Bsd-mediated activation is indirect. Bsd physically interacts with Map205 (Fig. 4A), and Bsd could phosphorylate Map205 to release Polo from microtubules, while an unknown kinase directly activates Polo. Alternatively, Map205 bound Polo can be directly phosphorylated by Aurora B, which releases Polo from Map205-mediated inhibition (Kachaner et al., 2014). It is possible that Bsd functions like Aurora B, and directly activates Map205 bound Polo in nascent myotubes.

Nuclear functions of Polo and Bsd

In S2 cell nuclei, Bsd and Polo localization was non-overlapping (Fig. S5E), which suggests that Bsd and Polo have independent roles in the nucleus. The most likely role for Polo in myonuclei is the nuclear export of Tum and Pav (Fig. 6H). Polo directly binds Tum and Pav (Ebrahimi et al., 2010; Somers and Saint, 2003), and Tum and Pav localize to the nucleus in S2 cells and post-mitotic embryonic cells (Jones et al., 2010). As microtubules reorganize in nascent myotubes, cytoplasmic Tum/Pav complexes presumably position the minus-end nucleator γ-tubulin. Similar to cytokinesis, where Polo functions to position Tum and Pav during furrow formation, activated Polo could direct the translocation of Tum/Pav from myonuclei to the cytoplasm to direct microtubule reorganization and myotube guidance.

The nuclear function of Bsd could involve preventing myotube-myotube fusion, which appears to act through a Tum-independent mechanism. The myotube fusion events we observed in *bsd*^{1} embryos occurred two hours after myotube guidance initiated (Movie 2), and were coincident with maximal Bsd enrichment in the nucleus (Fig. 2B). Myoblast fusion in Drosophila embryos is directional, meaning founder cells and nascent myotubes only fuse with fusion competent myoblasts. However, experimental conditions where founder cells fuse with other founder cells or myotubes fuse each other myotubes have not been reported. The mechanisms that regulate myoblast fusion involve cell-cell recognition molecules and cytoskeletal regulatory proteins, and Bsd physically interacted with two nuclear proteins, Imp and Mi-2, which regulate the expression of cytoskeletal proteins [(Fig. 4A) (Hansen et al., 2015; Medioni et al., 2014; Parrish et al., 2006)]. Bsd may therefore have nuclear substrates that ultimately prevent myotube fusion.

The nuclear translocation of Bsd could also serve a regulatory function. The proteins that activate VRKs are unknown, and our proteomics work did not identify any obvious candidates that would work upstream Bsd during myotube guidance. However, Ran GTPase and Aurora B are two nuclear proteins that inhibit VRK1 and VRK2 activity (Moura et al., 2018; Sanz-García et al., 2008). It is possible that nuclear translocation inactivates Bsd as a mechanism to limit Polo activation in the cytoplasm.

Specialized functions for Polo

Although Polo is a general regulator of mitotsis and meiosis, specialized roles for Polo have recently come to light. For example, Polo regulates asymmetric cell division of neuroblasts (Wang et al., 2007) and promotes neural stem cell development, maintenance, and lineage progression (Lee et al., 2016). Several screens have identified a genetic requirement for *polo* in

processes that could involve post-mitotic cells, but to our knowledge we have identified the first example in which Polo performs an essential function in post-mitotic cells. *Drosophila* embryos that are homozygous for hypomorphic *polo* alleles develop beyond nuclear division, cellularization, and gastrulation, presumably due to the maternal contribution of Polo (Figs. 4D-H, S4C,D). We are particularly excited that the embryo and early larva could serve as a robust platform to identify novel roles for Polo in tissue maturation and morphogenesis, and we suspect that such studies will uncover novel mechanisms and pathways that regulate Polo activation.

Non-centrosomal Microtubule Organizing Centers (ncMTOCs) and myotube guidance

While centrosomal MTOCs are the well-known, key regulators of microtubule assembly and dynamics during cell division, ncMTOCs are emerging as essential regulators of cellular morphogenesis across a variety of cell types including follicle cells, the salivary gland, tracheal cells, and myotubes (Tillery et al., 2018). The mechanisms that regulate ncMTOC assembly and function are incompletely understood, but a common feature of ncMTOCs is that proteins involved in microtubule dynamics and anchoring are localized to microtubule minus-ends. The current model for myogenic ncMTOCs is that perinuclear foci of γ-tubulin and the anchoring protein Ninein reorganize the microtubule cytoskeleton during myotube elongation and position the myonuclei in mature muscles (Guerin and Kramer, 2009b; Zheng et al., 2016). However, our data are consistent with a model in which non-perinuclear ncMTOCs develop in nascent myotubes to direct guidance. We found that γ-tubulin foci were not only perinuclear during myotube elongation, but were also concentrated toward myotube leading edges (Fig. 3D). In addition, the minus-end protein Nod formed stable linear arrays during LO1 myotube guidance (Fig. 3A,C; Movie 3), but the LO1 myonuclei were highly dynamic (Movie 1). In fact, LO1 myonuclei often moved in a direction opposite of the leading edge, which suggests that the stable arrangement of microtubule minus-ends must be anchored to site away from the myonuclei. Identifying the myotube ncMTOC anchoring proteins will be an essential next step in understanding the role of ncMTOCs during muscle morphogenesis.

Bsd is a conserved activator of Polo catalytic activity

Murine Vrk3 regulates myotube elongation, physically associates with Plk1, and promotes $Plk1^{T210}$ phosphorylation (Fig. 6A-G). The active site in human VRK3 is divergent at three residues, which led to the hypothesis that VRK3 is a pseudokinase (Scheeff et al., 2009). However, subsequent studies show that VRK3 has kinase activity under certain contexts (Park et al., 2015), and our studies support an active role for Vrk3 in promoting phosphorylation. In

fact, the conservation of Bsd/Vrk3 cellular and molecular functions is so striking that Vrk3 likely regulates Plk1 activity under a variety of developmental and homeostatic contexts.

Although Vrk3 has not been studied *in vivo*, Plk1 was recently shown to regulate myogenesis in mice. Muscle-specific deletion of *Plk1* blocked limb muscle development during embryogenesis and prevented muscle stem cells from activating after injury (Jia et al., 2019). However, it remains unclear how Plk1 is regulated during mammalian muscle development, what the targets of Plk1 are in the muscle lineage, and whether Plk1 regulates muscle morphogenesis. Our study highlights the exciting possibility that Vrk3 regulates Plk1 activity i*n vivo* and that the role of Plk1 during mammalian myogenesis extends well beyond cell cycle control.

Acknowledgements

We thank Helen McNeill and Mayssa Mokalled for critical reading of the manuscript, and the *Drosophila* community for stocks and reagents. ANJ was supported by NIH R01AR070299. PHT was supported by NIH R01MH067122.

Methods

Drosophila genetics

The *bsd*^{1} allele was recovered in an EMS screen as described (Johnson et al., 2013). The stocks used in this study include *Df(2R)BSC199*, *Df(2R)BSC699*, *polo*^{1}, *polo*^{KG03033}, *Df(3L)BSC447*, *tum*^{DH15}, *P{UAS-polo.T182D}, P{PTT-GC}polo*^{CC01326} (Polo-GFP), *P{Gal4-tey*^{5053A}*}, P{GMR40D04-GAL4}attP2* (*slou.Gal4*), *P{GMR57C12-GAL4}attP2* (*nau.Gal4*), *P{Gal4-how*^{24B}*}, P{UAS-Lifeact-RFP}, P{UAS-eGFP}* (Bloomington Stock Center), and *P{Gal4-kirre*^{rP298}*}, P{kirre*^{rP298}*.lacZ}* (Nose et al., 1998), *P{Gal4-Mef2}* (Ranganayakulu et al., 1998), and *P{MHC.τGFP}* (Chen et al., 2003). *Cyo, P{Gal4-Twi}, P{2X-UAS.eGFP}; Cyo, P{wg.lacZ}; TM3, P{Gal4-Twi}, P{2X-UAS.eGFP}; and TM3, P{ftz.lacZ}* balancers were used to genotype embryos.

Bsd transgenic flies were generated by subcloning the *bsd* coding sequence (LD23371, *Drosophila* Genomics Resource Center, supported by NIH grant 2P40OD010949) into pUASt-Attb (KpnI/XbaI). Site directed mutagenesis by PCR sewing was used to make UAS.Bsd.I129A. Plasmids and P(acman) BACs (CH321-61F090 and CH322-02P20) were injected and targeted to a ϕC31 integration site at 22A2 (Rainbow Transgenic Flies; Bloomington Stock 24481); stable insertions were identified by standard methods.

RNA sequencing and variant identification

Total RNA was collected from 12-24hr embryos per manufacturer's specification (RNeasy kit, Qiagen). cDNA libraries were generated with the TruSeq stranded mRNA sample library kit (Illumina) and sequenced using 50bp paired-end reads on the Illumina HiSeq 2000 system. Two technical replicates of *w*^{1118} and *bsd*^{1} were prepared and sequenced. Sequence reads were mapped to the *Drosophila* genome with Genomic Short-Read Nucleotide Alignment Program (GSNAP) using the Cufflinks method. Variants (single nucleotide variants and insertions/deletions) were identified with the Broad Institute's Genome Analysis Toolkit (GATK) as described (Baschal et al., 2015), and the resulting variants were functionally tested by complementation test. The *bsd*^{1} allele (Q545*) was confirmed with Sanger sequencing.

Bsd antibody

We created a fusion Bsd::6xHis fusion protein by PCR, using the C-terminus amino acids 705–1004 of Bsd. We sub-cloned the 598bp fragment into the pHO4d 6xHIS expression vector (Hadwiger et al., 2010) via conventional restriction enzyme sites. The Bsd 6xHIS fusion construct was transformed into competent BL21 (DE3) pLysS *E. coli* cells (Invitrogen) and grown, overnight shaking at 37°C in DYT supplemented with 100 µg/ml ampicillin. The cells were diluted 25 times in fresh DYT media and grown at 37°C to an OD_{600} = 0.6–0.7. We

added isopropyl β-D-thiogalactoside (IPTG) to 1 mM to induce expression of the fusion protein and incubated overnight shaking at 18°C. We purified the 6xHIS fusion protein on nickel-nitrilotriacetic acid agarose (Qiagen, Valencia, CA) according to the manufacturer's protocols, under native conditions with modified buffers and dialyzed against PBS. We sent the purified protein to Pocono Rabbit Farm & Laboratory (Canadensis, PA) for guinea pig custom polyclonal antibody production.

Plasmids and mutagenesis

Expression plasmids for the immunoprecipitation screen included the BDGP Flag-HA C-terminal fusions FMO03130 (Lost), FMO05923 (Map205), FMO06869 (Polo), FMO07294 (Imp), FMO11010 (Yp3), FMO12286 (Jar). Plasmids for expressing tagged proteins in S2 cells were generated by cloning coding sequences into pEntr/SD (Thermofisher, K242020), and recombining the coding sequences into pAc5 promoter destination vectors (pAWM and pAWF). Site directed mutagenesis was performed as described above to generate Bsd.Q545* and Polo.T182A. To generate GST-Bsd for *E. coli* expression, the *bsd* coding sequence was subcloned into pGex4T-1 (Sal1/NotI). The Vrk3 mammalian expression construct was generated by recombining pDONR223-VRK3 [Addgene 23687, (Johannessen et al., 2010)] into pDEST-CMV-3xFLAG-EGFP [Addgene 122845, (Agrotis and Pengo, 2019)]; pRcCMV-Myc-Plk1 was used without modification [Addgene 41160, (Golsteyn et al., 1994)].

Immunohistochemistry

Antibodies used include α-Mef2 (1:1000, gift from R. Cripps), α-Tropomyosin (1:600, Abcam, MAC141), α-PLK1-phospho-T210 (1:100, Abcam, ab39068), α-GFP (1:600, Torrey Pines Biolabs, TP-401), and α-βgal (1:100, Promega, Z3781). Embryo antibody staining was performed as described (Johnson et al., 2013); HRP-conjugated secondary antibodies in conjunction with the TSA system (Molecular Probes) were used to detect primary antibodies. For S2 cell labeling, cells ($5x10^6$) were transfected per manufacturer's specifications (Lipofectamine 3000, Invitrogen; applies to all transfections in this study), cultured at 25°C in Schneider's Drosophila medium (Sigma, S9895) supplemented with 10% heat-inactivated fetal bovine serum (FBS, Invitrogen, 10082147) for 72h, collected and washed once with S2 medium. Cells were then seeded into a 6-well-plate with a glass cover slip and incubated for 1h. The cells were washed twice with PBS and fixed with 4% PFA for 15min, and then washed 3 times with PBS. After 1h blocking in 25%NGS/PBST, cells were incubated with α-FLAG antibody (1:1000, Sigma, F3165) and α-Myc antibody (1:1000, Sigma, PLA001) in PBST containing 0.5% BSA at 4°C for 12h. After five PBS washes, cells were mounted in Vectashield with DAPI (H-1000).

Imaging and image analysis

Embryos were imaged with a Zeiss LSM800 confocal microscope; cells were imaged by confocal or with an inverted Zeiss AxioObserver. For time-lapse imaging, dechorionated St12 embryos were mounted in halocarbon oil and scanned at 6min intervals. For single-frame live imaging, embryos were dechorionated, mounted in PBT, and directly scanned. Control and mutant embryos were prepared and imaged in parallel where possible, and imaging parameters were maintained between genotypes. Fluorescent intensity and cell morphology measurements were made with ImageJ software.

Immunoprecipitation and Western blotting

For *Drosophila* proteins, S2 cells ($8x10^6$) were transfected with 2μg of each plasmid in 6-well plates. Cells were cultured for 48h, incubated with 2mM $CuSO_4$ for 24h (for FMO plasmids only), collected, washed twice with PBS, lysed with 600μl IP buffer (20 mM Hepes, pH=7.4, 150 nM NaCl, 1% NP40, 1.5 mM $MgCl_2$, 2 mM EGTA, 10 mM NaF, 1 mM Na_3VO_4, 1X proteinase inhibitor), incubated on ice for 30 min, centrifuged at 12000Xg for 15min. The supernatant was collected, incubated with 2μl α-FLAG (Sigma, F3165) or α-Myc (PLA001, Sigma) overnight at 4°C, and then incubated with 50μl Dynabeads (Invitrogen, 10007D) for 4hr at 4°C. The beads were washed 3X with IP buffer, and immunoblotted with α-Myc (1:3000) or α-FLAG (1:2000).

For *in vitro* phosphorylation assays, immunoprecipitation was carried out as described, except that anti-Phosphothreonine antibody (1:125, Abcam, ab9337) was used for immunoblotting. For *in vivo* phosphorylation assays, 200 *Polo-GFP* and 200 *bsd*[1]; *Polo-GFP* embryos were homogenized in 600μl IP buffer, large debris was removed by 15min centrifugation (12,000Xg), and immunoprecipitation was carried out as described above using 2μl α-GFP (Torrey Pines Biolabs, TP-401).

For mammalian proteins, HEK293T cells were seeded in 6-well plates, grown to 60% confluency at 37°C and 5%CO_2 in Dulbecco's modified Eagle's medium (DMEM; Invitrogen) supplemented with 10% heat-inactivated FBS. Cells were transfected with 2μg of each plasmid and cultured for 48h. Immunoprecipitations were carried out as described above. Plk1 phosphorylation was directly assayed without immunoprecipitation using α-PLK1-phospho-T210 (1:500, Abcam, ab39068).

Western blots were performed by standard method using precast gels (456-1096, BioRad), and imaged with the ChemiDoc XRS+ system (BioRad).

siRNA knockdown and inhibitor treatments

For siRNAs, C2C12 cells were seeded in 6-well-plate and grown in standard conditions to 60% confluency in growth medium (10% FBS in DMEM), and transfected 10 nM duplexed 27nt siRNAs (Integrated DNA Technologies). Transfection efficiency was monitored with Cy3 transfection controls (Trifecta Kit, Integrated DNA Technologies). After 24hr, the growth media was changed to differentiation media (2% horse serum in DMEM). After 7 days differentiation, cells were fixed for 15min in 4% PFA and stained with α-alpha-actinin antibody (A7811, Sigma, 1:1000).

For Volasertib, C2C12 cells were seeded in 6-well-plate and grown in standard conditions to nearly 100% confluency in growth medium, and treated with 100nM Volasertib or DMSO for 24h in growth medium (No.S2235, Selleck chem). Then the growth medium was changed to differentiation medium (2% horse serum in DMEM), with 100nM Volasertib or DMSO and incubated for 48h. Cells were incubated in differentiation medium without Volasertib or DMSO for additional 5 days, fixed and stained as described above.

Bioinformatic and statistical analysis

Protein alignments were generated in ClustalX (Larkin et al., 2007), and phylogenetic analyses were performed with DNAMAN (Lynnon Corporation) using the observed divergency distance method. ATPbind (Hu et al., 2018) was used to predict Bsd ATP binding residues; informatics predictions were compared to the VRK1 ATP binding pocket described in (Shin et al., 2011).

Statistical analyses were performed with GraphPad Prism 8 software, and significance was determined with the unpaired, one-tailed student's t-test or Mann-Whitney test (for non-Gaussain distributions). Gaussian distribution fit curve and skew distribution fit curve were generated wtih Origin 2019 software. Sample sizes are indicated in the figure legends. Data collection and data analysis were routinely performed by different authors to prevent potential bias. All individuals were included in data analysis.

References

Adams, R.H., and Eichmann, A. (2010). Axon guidance molecules in vascular patterning. Cold Spring Harbor perspectives in biology *2*, a001875.

Adams, R.R., Tavares, A.A., Salzberg, A., Bellen, H.J., and Glover, D.M. (1998). pavarotti encodes a kinesin-like protein required to organize the central spindle and contractile ring for cytokinesis. Genes & development *12*, 1483-1494.

Agrotis, A., and Pengo, N. (2019). Redundancy of human ATG4 protease isoforms in autophagy and LC3/GABARAP processing revealed in cells. *15*, 976-997.

Archambault, V., D'Avino, P.P., Deery, M.J., Lilley, K.S., and Glover, D.M. (2008). Sequestration of Polo kinase to microtubules by phosphopriming-independent binding to Map205 is relieved by phosphorylation at a CDK site in mitosis. Genes & development *22*, 2707-2720.

Baschal, E.E., Wethey, C.I., Swindle, K., Baschal, R.M., Gowan, K., Tang, N.L.S., Alvarado, D.M., Haller, G.E., Dobbs, M.B., Taylor, M.R.G.*, et al.* (2015). Exome Sequencing Identifies a Rare HSPG2 Variant Associated with Familial Idiopathic Scoliosis. G3: Genes|Genomes|Genetics *5*, 167.

Best, B.T. (2019). Single-cell branching morphogenesis in the Drosophila trachea. Developmental biology *451*, 5-15.

Bonner, A.M., Hughes, S.E., and Hawley, R.S. (2020). Regulation of Polo Kinase by Matrimony Is Required for Cohesin Maintenance during Drosophila melanogaster Female Meiosis. Current Biology *30*, 715-722.e713.

Buszczak, M., Paterno, S., Lighthouse, D., Bachman, J., Planck, J., Owen, S., Skora, A.D., Nystul, T.G., Ohlstein, B., Allen, A.*, et al.* (2007). The Carnegie protein trap library: A versatile tool for Drosophila developmental studies. Genetics *175*, 1505-1531.

Cabral, G., Laos, T., Dumont, J., and Dammermann, A. (2019). Differential Requirements for Centrioles in Mitotic Centrosome Growth and Maintenance. Developmental cell *50*, 355-366.e356.

Carmena, M., Pinson, X., Platani, M., Salloum, Z., Xu, Z., Clark, A., Macisaac, F., Ogawa, H., Eggert, U., Glover, D.M.*, et al.* (2012). The chromosomal passenger complex activates polo kinase at centromeres. PLoS Biology *10*, e1001250.

Carmena, M., Riparbelli, M.G., Minestrini, G., Tavares, A.M., Adams, R., Callaini, G., and Glover, D.M. (1998). Drosophila polo kinase is required for cytokinesis. The Journal of cell biology *143*, 659-671.

Chen, E.H., Pryce, B.A., Tzeng, J.A., Gonzalez, G.A., and Olson, E.N. (2003). Control of myoblast fusion by a guanine nucleotide exchange factor, loner, and its effector ARF6. Cell *114*, 751-762.

D'Avino, P.P., Savoian, M.S., Capalbo, L., and Glover, D.M. (2006). RacGAP50C is sufficient to signal cleavage furrow formation during cytokinesis. Journal of Cell Science *119*, 4402-4408.

Donaldson, M.M., Tavares, A.A., Ohkura, H., Deak, P., and Glover, D.M. (2001). Metaphase arrest with centromere separation in polo mutants of Drosophila. The Journal of cell biology *153*, 663-676.

Ebrahimi, S., Fraval, H., Murray, M., Saint, R., and Gregory, S.L. (2010). Polo kinase interacts with RacGAP50C and is required to localize the cytokinesis initiation complex. Journal of Biological Chemistry *285*, 28667-28673.

El-Bazzal, L., Rihan, K., Bernard-Marissal, N., Castro, C., Chouery-Khoury, E., Desvignes, J.P., Atkinson, A., Bertaux, K., Koussa, S., Lévy, N.*, et al.* (2019). Loss of Cajal bodies in motor neurons from patients with novel mutations in VRK1. Human molecular genetics *28*, 2378-2394.

Fu, J., and Lipinszki, Z. (2016). Conserved molecular interactions in centriole-to-centrosome conversion. *18*, 87-99.

Golsteyn, R.M., Schultz, S.J., Bartek, J., Ziemiecki, A., Ried, T., and Nigg, E.A. (1994). Cell cycle analysis and chromosomal localization of human Plk1, a putative homologue of the mitotic kinases Drosophila polo and Saccharomyces cerevisiae Cdc5. J Cell Sci *107 (Pt 6)*, 1509-1517.

Greenbaum, L., Barel, O., Nikitin, V., Hersalis-Eldar, A., Kol, N., Reznik-Wolf, H., Dominissini, D., Pras, E., and Dori, A. (2020). Identification of a homozygous VRK1 mutation in two patients with adult-onset distal hereditary motor neuropathy. Muscle & nerve *61*, 395-400.

Gregory, S.L., Ebrahimi, S., Milverton, J., Jones, W.M., Bejsovec, A., and Saint, R. (2008). Cell division requires a direct link between microtubule-bound RacGAP and Anillin in the contractile ring. Current Biology *18*, 25-29.

Guerin, C.M., and Kramer, S.G. (2009a). Cytoskeletal remodeling during myotube assembly and guidance: coordinating the actin and microtubule networks. Communicative & integrative biology *2*, 452-457.

Guerin, C.M., and Kramer, S.G. (2009b). RacGAP50C directs perinuclear gamma-tubulin localization to organize the uniform microtubule array required for Drosophila myotube extension. Development *136*, 1411-1421.

Hadwiger, G., Dour, S., Arur, S., Fox, P., and Nonet, M.L. (2010). A monoclonal antibody toolkit for C. elegans. PloS one *5*, e10161.

Hansen, H.T., Rasmussen, S.H., Adolph, S.K., Plass, M., Krogh, A., Sanford, J., Nielsen, F.C., and Christiansen, J. (2015). Drosophila Imp iCLIP identifies an RNA assemblage coordinating F-actin formation. Genome Biology *16*, 123.

Herzig, B., Yakulov, T.A., Klinge, K., Gunesdogan, U., Jackle, H., and Herzig, A. (2014). Ballchen is required for self-renewal of germline stem cells in Drosophila melanogaster. Biol Open *3*, 510-521.

Hu, J., Li, Y., Zhang, Y., and Yu, D.J. (2018). ATPbind: Accurate Protein-ATP Binding Site Prediction by Combining Sequence-Profiling and Structure-Based Comparisons. Journal of chemical information and modeling *58*, 501-510.

Jang, Y.-J., Lin, C.-Y., Ma, S., and Erikson, R.L. (2002). Functional studies on the role of the C-terminal domain of mammalian polo-like kinase. Proceedings of the National Academy of Sciences *99*, 1984.

Jia, Z., Nie, Y., Yue, F., Kong, Y., Gu, L., Gavin, T.P., Liu, X., and Kuang, S. (2019). A requirement of Polo-like kinase 1 in murine embryonic myogenesis and adult muscle regeneration. *8*.

Johannessen, C.M., Boehm, J.S., Kim, S.Y., Thomas, S.R., Wardwell, L., Johnson, L.A., Emery, C.M., Stransky, N., Cogdill, A.P., Barretina, J.*, et al.* (2010). COT drives resistance to RAF inhibition through MAP kinase pathway reactivation. Nature *468*, 968-972.

Johnson, A.N., Mokalled, M.H., Valera, J.M., Poss, K.D., and Olson, E.N. (2013). Post-transcriptional regulation of myotube elongation and myogenesis by Hoi Polloi. Development *140*, 3645-3656.

Jones, W.M., Chao, A.T., Zavortink, M., Saint, R., and Bejsovec, A. (2010). Cytokinesis proteins Tum and Pav have a nuclear role in Wnt regulation. J Cell Sci *123*, 2179-2189.

Kachaner, D., Garrido, D., Mehsen, H., Normandin, K., Lavoie, H., and Archambault, V. (2017). Coupling of Polo kinase activation to nuclear localization by a bifunctional NLS is required during mitotic entry. Nature communications *8*, 1701.

Kachaner, D., Pinson, X., El Kadhi, K.B., Normandin, K., Talje, L., Lavoie, H., Lépine, G., Carréno, S., Kwok, B.H., Hickson, G.R.*, et al.* (2014). Interdomain allosteric regulation of Polo kinase by Aurora B and Map205 is required for cytokinesis. The Journal of cell biology *207*, 201-211.

Kramer, S.G., Kidd, T., Simpson, J.H., and Goodman, C.S. (2001). Switching repulsion to attraction: changing responses to slit during transition in mesoderm migration. Science *292*, 737-740.

Lane, H.A., and Nigg, E.A. (1996). Antibody microinjection reveals an essential role for human polo-like kinase 1 (Plk1) in the functional maturation of mitotic centrosomes. The Journal of cell biology *135*, 1701-1713.

Larkin, M.A., Blackshields, G., Brown, N.P., Chenna, R., McGettigan, P.A., McWilliam, H., Valentin, F., Wallace, I.M., Wilm, A., Lopez, R.*, et al.* (2007). Clustal W and Clustal X version 2.0. Bioinformatics *23*, 2947-2948.

Lee, S., Lee, K.S., Huh, S., Liu, S., Lee, D.Y., Hong, S.H., Yu, K., and Lu, B. (2016). Polo Kinase Phosphorylates Miro to Control ER-Mitochondria Contact Sites and Mitochondrial Ca(2+) Homeostasis in Neural Stem Cell Development. Developmental cell *37*, 174-189.

Lénárt, P., Petronczki, M., Steegmaier, M., Di Fiore, B., Lipp, J.J., Hoffmann, M., Rettig, W.J., Kraut, N., and Peters, J.-M. (2007). The Small-Molecule Inhibitor BI 2536 Reveals Novel Insights into Mitotic Roles of Polo-like Kinase 1. Current Biology *17*, 304-315.

Liu, D., Davydenko, O., and Lampson, M.A. (2012). Polo-like kinase-1 regulates kinetochore–microtubule dynamics and spindle checkpoint silencing. Journal of Cell Biology *198*, 491-499.

Liu, X., and Erikson, R.L. (2002). Activation of Cdc2/cyclin B and inhibition of centrosome amplification in cells depleted of Plk1 by siRNA. Proceedings of the National Academy of Sciences of the United States of America *99*, 8672-8676.

Martín-Doncel, E., and Rojas, A.M. (2019). VRK1 functional insufficiency due to alterations in protein stability or kinase activity of human VRK1 pathogenic variants implicated in neuromotor syndromes. *9*, 13381.

McCormick, L.E., and Gupton, S.L. (2020). Mechanistic advances in axon pathfinding. Current opinion in cell biology *63*, 11-19.

Medioni, C., Ramialison, M., Ephrussi, A., and Besse, F. (2014). Imp Promotes Axonal Remodeling by Regulating profilin mRNA during Brain Development. Current Biology *24*, 793-800.

Moura, D.S., Campillo-Marcos, I., Vázquez-Cedeira, M., and Lazo, P.A. (2018). VRK1 and AURKB form a complex that cross inhibit their kinase activity and the phosphorylation of histone H3 in the progression of mitosis. *75*, 2591-2611.

Nichols, R.J., Wiebe, M.S., and Traktman, P. (2006). The vaccinia-related kinases phosphorylate the N' terminus of BAF, regulating its interaction with DNA and its retention in the nucleus. Molecular biology of the cell *17*, 2451-2464.

Nose, A., Isshiki, T., and Takeichi, M. (1998). Regional specification of muscle progenitors in Drosophila: the role of the msh homeobox gene. Development *125*, 215-223.

Novak, Z.A., Wainman, A., Gartenmann, L., and Raff, J.W. (2016). Cdk1 Phosphorylates Drosophila Sas-4 to Recruit Polo to Daughter Centrioles and Convert Them to Centrosomes. Developmental cell *37*, 545-557.

Park, C.H., Ryu, H.G., Kim, S.H., Lee, D., Song, H., and Kim, K.T. (2015). Presumed pseudokinase VRK3 functions as a BAF kinase. Biochimica et biophysica acta *1853*, 1738-1748.

Parrish, J.Z., Kim, M.D., Jan, L.Y., and Jan, Y.N. (2006). Genome-wide analyses identify transcription factors required for proper morphogenesis of Drosophila sensory neuron dendrites. Genes & development *20*, 820-835.

Ranganayakulu, G., Elliott, D.A., Harvey, R.P., and Olson, E.N. (1998). Divergent roles for NK-2 class homeobox genes in cardiogenesis in flies and mice. Development *125*, 3037-3048.

Renbaum, P., Kellerman, E., Jaron, R., Geiger, D., Segel, R., Lee, M., King, M.C., and Levy-Lahad, E. (2009). Spinal muscular atrophy with pontocerebellar hypoplasia is caused by a mutation in the VRK1 gene. American journal of human genetics *85*, 281-289.

Sanz-García, M., López-Sánchez, I., and Lazo, P.A. (2008). Proteomics identification of nuclear Ran GTPase as an inhibitor of human VRK1 and VRK2 (vaccinia-related kinase) activities. Molecular & cellular proteomics : MCP *7*, 2199-2214.

Scheeff, E.D., Eswaran, J., Bunkoczi, G., Knapp, S., and Manning, G. (2009). Structure of the pseudokinase VRK3 reveals a degraded catalytic site, a highly conserved kinase fold, and a putative regulatory binding site. Structure *17*, 128-138.

Schnorrer, F., and Dickson, B.J. (2004). Muscle building; mechanisms of myotube guidance and attachment site selection. Developmental cell *7*, 9-20.

Schnorrer, F., Kalchhauser, I., and Dickson, B.J. (2007). The transmembrane protein Kon-tiki couples to Dgrip to mediate myotube targeting in Drosophila. Developmental cell *12*, 751-766.

Schnorrer, F., Schönbauer, C., Langer, C.C.H., Dietzl, G., Novatchkova, M., Schernhuber, K., Fellner, M., Azaryan, A., Radolf, M., Stark, A.*, et al.* (2010). Systematic genetic analysis of muscle morphogenesis and function in Drosophila. Nature *464*, 287-291.

Schober, C.S., Aydiner, F., Booth, C.J., Seli, E., and Reinke, V. (2011). The kinase VRK1 is required for normal meiotic progression in mammalian oogenesis. Mechanisms of development *128*, 178-190.

Sevilla, A., Santos, C.R., Barcia, R., Vega, F.M., and Lazo, P.A. (2004). c-Jun phosphorylation by the human vaccinia-related kinase 1 (VRK1) and its cooperation with the N-terminal kinase of c-Jun (JNK). Oncogene *23*, 8950-8958.

Shin, J., Chakraborty, G., Bharatham, N., Kang, C., Tochio, N., Koshiba, S., Kigawa, T., Kim, W., Kim, K.T., and Yoon, H.S. (2011). NMR solution structure of human vaccinia-related kinase 1 (VRK1) reveals the C-terminal tail essential for its structural stability and autocatalytic activity. The Journal of biological chemistry *286*, 22131-22138.

Somers, W.G., and Saint, R. (2003). A RhoGEF and Rho family GTPase-activating protein complex links the contractile ring to cortical microtubules at the onset of cytokinesis. Developmental cell *4*, 29-39.

Stoll, M., Teoh, H., Lee, J., Reddel, S., Zhu, Y., Buckley, M., Sampaio, H., Roscioli, T., Farrar, M., and Nicholson, G. (2016). Novel motor phenotypes in patients with VRK1 mutations without pontocerebellar hypoplasia. Neurology.

Tillery, M.M.L., Blake-Hedges, C., Zheng, Y., Buchwalter, R.A., and Megraw, T.L. (2018). Centrosomal and Non-Centrosomal Microtubule-Organizing Centers (MTOCs) in Drosophila melanogaster, pp. E121.

Vega, F.M., Sevilla, A., and Lazo, P.A. (2004). p53 Stabilization and accumulation induced by human vaccinia-related kinase 1. Molecular and cellular biology *24*, 10366-10380.
Wang, H., Ouyang, Y., Somers, W.G., Chia, W., and Lu, B. (2007). Polo inhibits progenitor self-renewal and regulates Numb asymmetry by phosphorylating Pon. Nature *449*, 96-100.
Wiebe, M.S., Nichols, R.J., Molitor, T.P., Lindgren, J.K., and Traktman, P. (2010). Mice deficient in the serine/threonine protein kinase VRK1 are infertile due to a progressive loss of spermatogonia. Biology of reproduction *82*, 182-193.
Williams, J., Boin, N.G., Valera, J.M., and Johnson, A.N. (2015). Noncanonical roles for Tropomyosin during myogenesis. Development *142*, 3440-3452.
Yakulov, T., Gunesdogan, U., Jackle, H., and Herzig, A. (2014). Ballchen participates in proliferation control and prevents the differentiation of Drosophila melanogaster neuronal stem cells. Biol Open *3*, 881-886.
Yang, S., Weske, A., Du, Y., Valera, J.M., Jones, K.L., and Johnson, A.N. (2020). FGF signaling directs myotube guidance by regulating Rac activity. Development *147*.
Zheng, Y., Mennella, V., Marks, S., Wildonger, J., Elnagdi, E., Agard, D.A., and Megraw, T.L. (2016). The Seckel syndrome and centrosomal protein Ninein localizes asymmetrically to stem cell centrosomes but is not required for normal development, behavior, or DNA damage response in Drosophila. Molecular biology of the cell *27*, 1740-1752.

Figure Legends

Figure 1. The ser/thr kinase Bsd regulates muscle morphogenesis. (A) Experimental design to identify novel regulators of myogenesis. (B) Muscle morphogenesis phenotype in *bsd*^{1} mutants. Stage 16 embryos labeled with Tropomyosin. DT1 and LO1 muscles are pseudocolored orange and green. Control (*w*^{1118}) embryos showed a stereotypic pattern of body wall muscles. *bsd*^{1} embryos showed severe defects in muscle morphology, including rounded and bent muscles; a number of muscles were also missing. The *bsd*^{1} myogenic defects were completely rescued in embryos harboring one of two overlapping genomic constructs (CH322-02P20 or CH321-61F090). Outcrossing CH321-61F090 restored the *bsd*^{1} myogenic phenotype. (C) Quantification of muscle phenotypes. Individual muscles were scored in segments A2-A8 of St16 embryos; the frequencies of muscle defects are shown as a heat map of the stereotypic muscle pattern in an embryonic segment. (D) Genetic mapping details and the Bsd protein domains. Two overlapping deficiencies failed to complement *bsd*^{1} (dashed lines indicate breakpoints outside the genomic region shown; see Fig. S1 for transheterozygous phenotypes). The Bsd protein has a kinase domain (KD; green) that is conserved among the VRK protein family; the Bsd KD is divided by a unique linker. VRK proteins have highly variable C-termini (see Fig. S1 for protein alignments). The position of the conserved ATP binding pocket is also shown (purple). (E) *bsd*^{1} VL1 muscle phenotype. Stage 16 embryos labeled for *5053>GFP* (green) and Tropomyosin (violet). *bsd*^{1} VL1 muscles were rounded (blue arrowhead) and made incorrect or incomplete tendon attachments (white arrowheads). (F) *bsd*^{1} DT1, LO1, and VT1 muscle phenotypes. Stage 16 embryos labeled for *slou>GFP* (green) and Tropomyosin (violet). *bsd*^{1} DT1, LO1, and VT1 muscles made incorrect tendon attachments (white arrowheads; see Movie 1) or remained round (blue arrowhead). (G) Histogram of VL1, DT1, LO1, and VT1 phenotypes (n≥54 per muscle). (H) Phenotype quantification. Muscles were individually scored normal=0, missing=3, elongation=2, attachment=1. Final muscle score = sum of phenotypic scores/number of embryos. (I) Myonuclei quantification in *bsd*^{1} embryos. The number of *rp298.lacZ* positive myonuclei per segment were counted in control and *bsd*^{1} embryos at three embryonic stages. The relative number of myonuclei in *bsd*^{1} embryos was reduced during myogenesis compared to controls. **($p<0.01$), ****($p<0.0001$). Error bars represent SEM.

Figure 2. Bsd functions in the mesoderm to direct myotube guidance and shows dynamic localization during myogenesis and. (A) Bsd acts cell autonomously during myogenesis. Control (*w*^{1118}), *bsd*^{1}*/Df(2R)BSC199 UAS.Bsd*, *bsd*^{1}*/Df(2R)BSC199 24B.Gal4>Bsd,* and *bsd*^{1}*/Df(2R)BSC199 24B.Gal4>Bsd.I129A* embryos labeled for Tropomyosin. DT1, LO1, and

VL1 muscles are pseudocolored orange, green, and violet. *bsd*^{1} embryos that expressed wild-type Bsd in the mesoderm showed improved muscle morphology, whereas *bsd*^{1} embryos that expressed catalytically inactive Bsd.I129A showed extensive muscle defects. Quantification of myogenic phenotypes is as described in Fig. 1. A diagram Bsd is shown with the predicted ATP binding pocket residues colored; I129 is shaded red. (B) Bsd is enriched in myonuclei during myotube guidance, but shows an even cellular distribution after muscle attachment. *w*^{1118} embryos immunolabeled for Bsd (green) and Mef2 (violet). In Stage 11-14 embryos, Bsd was enriched in Mef2+ myonuclei. By Stage 16, the distribution of Bsd was equivalent between myonuclei and the cytoplasm.

Figure 3. Microtubule reorganization during myotube guidance requires Bsd. (A-C) Live imaging stills of LO1 myotubes in Stage 12-15 embryos that expressed Nod.GFP (green), which localizes to microtubule minus ends, and LifeAct.RFP (violet), which localizes to F-actin. Transgene expression was controlled by *slou.Gal4*. Live imaging initiated once Nod.GFP fluorescence was detectable (0min). Control LO1 myotubes showed a linear array of microtubule minus ends at the onset of imaging (white arrowheads). Nod.GFP did not co-localize with F-actin at the myotube leading edges (white arrows), which is indicative of microtubules in a minus-ends-in conformation. The linear configuration of microtubule minus ends in *bsd*^{1} LO1 myotubes was delayed; Nod.GFP remained cortical through the early stages of myotube elongation (blue arrowheads). *bsd*^{1} microtubule minus ends often overlapped with the F-actin domain (red arrowhead). (B) LO1 myotubes from (A) showing F-actin expression by heat map. Scale bar represents detection range. F-actin levels were equivalent in control and *bsd*^{1} myotubes. (C) Quantification of Nod.GFP distribution. GFP fluorescence was traced in each frame of three independent live imaging experiments per genotype. Nod.GFP localization was stable in control myotubes, with a low roundness score (more linear) and an angle consistent with the final LO1 attachment angle. *bsd*^{1} myotubes showed fluctuating Nod.GFP localization, with an overall high roundness score (more cortical) and an angle that deviates from the control attachment angle. (D) Single confocal scans of multinucleate LO1 myotubes from Stage 12 *slou>GFP* embryos labeled for γ-tubulin (green), GFP (violet) and DAPI (blue). Control (*bsd*^{1}*/Cyo*) myotubes showed both cortical and internal cytoplasmic γ-tubulin foci, with internal foci concentrated toward the myotube leading edges (red arrowheads). *bsd*^{1} myotubes had significantly fewer internal γ-tubulin foci compared to controls, but an equivalent number of cortical γ-tubulin foci. Heat map scale is the same as in (B). (E) Quantification of γ-tubulin foci in

multinucleate Stage 12 myotubes. Embryos used for (D,E) were derived from the same preparation. (ns) not significant. **(p<0.01). Error bars represent SEM.

Figure 4. Bsd and Polo kinase are in a common myogenic pathway. (A) Heat map of Bsd AP-MS. Proteins from 12-24hr embryo lysates were affinity purified with control or Bsd-bound GST beads. Relative abundance was determined by MS. (B-C) Immunoprecipitation of S2 cell lysates transfected with Bsd, Bsd.Q545*, and Polo. Full length Bsd bound Polo in reciprocal experiments, but Bsd.Q545* did not interact with Polo. (D) *polo*^{1} VL1 muscle phenotype. Stage 16 embryos labeled for *5053>GFP* (green) and Tropomyosin (violet). *polo*^{1} VL1 muscles were rounded (blue arrowhead) and made incorrect or incomplete tendon attachments (white arrowheads). (E) *polo*^{1} DT1, LO1, and VT1 muscle phenotypes. Stage 16 embryos labeled for *slou>GFP* (green) and Tropomyosin (violet). *polo*^{1} LO1 muscles made incorrect tendon attachments (white arrowheads). (F) Muscle morphogenesis phenotypes in *bsd*^{1} *polo*^{1} double mutants. Stage 16 embryos labeled with Tropomyosin. DT1, LO1, and VL1 muscles are pseudocolored orange, green, and violet. The frequency and severity of muscle morphology defects was comparable between *bsd*^{1} and *bsd*^{1} *polo*^{1} embryos. Quantification of muscle phenotypes is as described in Fig. 1. (G) DT1, LO1, and VT1 phenotypes in *bsd*^{1} *polo*^{1} double mutant embryos (labeled as in E). The frequency and severity of DT1, LO1, and VT1 phenotypes was comparable between *bsd*^{1} and *bsd*^{1} *polo*^{1} embryos. (H) Quantification of DT1, LO1, and VT1 phenotypes. **(p<0.01), ****(p<0.0001). Error bars represent SEM.

Figure 5. Bsd activates Polo to regulate myotube guidance. (A) *in vitro* phosphorylation assays. Polo was immunoprecipitated from S2 cell lysates and blotted with a phospho-threonine (pThr) antibody. Cells transfected with Bsd showed more phosphorylated Polo than controls. (B) Polo localization in S2 cells. Bsd.Myc, Polo.Flag, and Polo.T182A.Flag were transfected into S2 cells; transgenic proteins were detected with anti-Myc (red, Bsd) and anti-Flag (green, Polo). Polo localized to discrete nuclear foci in a subset of control cells (middle column). The frequency of cells showing nuclear Polo foci was increased when Bsd was co-transfected with Polo (left column and graph). Cells transfected with Polo that lacked a phosphorylated threonine (T182A) showed no nuclear Polo foci (right column and graph). (C) Polo acts downstream of Bsd during myogenesis. *bsd*^{1} *UAS.Polo.T182D* and *bsd*^{1} *Mef2.Gal4>Polo.T182D* embryos labeled for Tropomyosin. DT1, LO1, and VL1 muscles are pseudocolored orange, green, and violet. Expressing active (phosphomimetic) Polo^{T182D} in the mesoderm of *bsd*^{1} embryos suppressed the *bsd*^{1} myogenic phenotype. Quantification of myogenic phenotypes is as

described in Fig. 1. (D) *in vivo* phosphorylation assays. Endogenous GFP-tagged Polo was immunoprecipitated from embryo lysates and blotted with pThr. *bsd*^{1} embryo lysates showed significantly less phosphorylated Polo than controls. (E) Stage 12 embryos immunolabeled for phosphorylated Polo (Polo^{pT182}, green) and Mef2 (violet). Polo^{pT182} localized to myonuclei in control embryos. (F) Polo^{pT182} levels in myonuclei were significantly reduced in *bsd*^{1} embryos. (G) *tum*^{DH15} VL1, DT1, LO1, and VT1 muscle phenotypes. Stage 16 embryos labeled for *5053>GFP* (green) and Tropomyosin (violet) or *slou>GFP* (green) and Tropomyosin (violet). *tum*^{DH15} muscles made incorrect tendon attachments similar to *bsd*^{1} muscles (white arrowheads). (H) Histogram of VL1, DT1, LO1, and VT1 phenotypes (n≥54 per muscle). (ns) not significant, **(p<0.01), ****(p<0.0001). Error bars represent SEM.

Figure 6. The Bsd orthologue Vrk3 is required for myotube elongation. (A) C2C12 cells treated with siRNAs against murine Vrk3 or with an inhibitor of Plk1 (Volasterib, 100nM). Cells were fixed after 7 days in differentiation media and labeled for α-actinin (green) to detect differentiated myotubes and DAPI (blue) to visualize myonuclei. Vrk3 knockdown and Volasterib treated myotubes were shorter than controls and often rounded. (B) Quantification of cumulative myotube length. (C) Myotube length distribution. Solid line showed the Gaussian distribution fit curve (blue) and skew distribution fit curve (red). (D) Individual myotubes were traced to determine a roundness score. Vrk3 RNAi and Volasterib treated myotubes showed a higher roundness score, indicating increased circularity. (E) Fusion index. Each data point represents the fusion index for a single field of view at 200X magnification. Vrk3 RNAi treated cells showed a lower fusion index compared to controls, whereas Volasterib treated cells showed an equivalent fusion index. (F) Immunoprecipitation of HEK293 cell lysates transfected with Vrk3 and Plk1 showed a physical interaction between Vrk3 and Plk1. Full length Bsd bound Polo in reciprocal experiments, but Bsd.Q545* did not interact with Polo. (G) Western blot HEK293 cell lysates transfected with Vrk3 and Plk1. Vrk3 promoted Plk1 phosphorylation. (H) Model of the Bsd-Polo myogenic pathway (see text for details). **(p<0.01), ****(p<0.0001), ns (no significance). Error bars represent SEM.

Movie Captions.

Movie 1. Bsd regulates myotube guidance. Live imaging of LO1 myotubes from Stage 12 *slou>eGFP,nRFP* embryos. *bsd*^{1} myotubes failed to elongate anteriorly and attached at the posterior of the segment. GFP (green), RFP (violet). Arrowheads denote the myotube dorsal leading edge.

Movie 2. Bsd prevents myotube-myotube fusion. Live imaging of LO1 myotubes from Stage 12 *slou>eGFP,nRFP* embryos. Multinucelate *bsd*^{1} myotubes occasionally fused. GFP (green), RFP (violet). Arrowheads track nuclei from distinct myotubes before and after fusion.

Movie 3. Microtubule reorganization is delayed in *bsd*^{1} myotubes. Live imaging of LO1 myotubes from Stage 12 *slou>Nod.GFP,LifeAct.RFP* embryos. Nod.GFP localizes to microtubule minus-ends. The formation of linear minus-end arrays was delayed in *bsd*^{1} myotubes. GFP (green), RFP (violet).

Supplemental Figure Legends

Figure S1, related to Figure 1. (A) *bsd* deficiency mapping. Live Stage 16 embryos that expressed Myosin Heavy Chain (MHC.GFP). *bsd*^{1}/*Df(2R)BSC199* and *bsd*^{1}/*Df(2R)BSC699* embryos phenocopied *bsd*^{1} embryos. A control (*w*^{1118}) embryo is shown for comparison. (B) Phylogenetic analysis of human, mouse, and fly Vrk proteins. The homology tree was generated using observed divergency as the distance method. The percent homology among species is shown (C) Protein alignment of the Vrk proteins from (B); black shading shows identical residues in all species, pink shading shows residues that are the same in most species, blue shading shows residues that are the same in at least 50% of species. The position of the *bsd*^{1} Q545* mutation is shown. Residues in the previously defined Kinase Domain (orange line) and ATP binding pocket (violet) for human Vrk1 are shown. Note that the Bsd kinase domain is split by a unique linker region, and that the C-termini of the Vrk proteins show low sequence homology. (D) Stage 12 *5053>GFP* embryos labeled for GFP. Control and *bsd*^{1} embryos showed an equivalent number of VL1 founder cells. (E) Stage 12 *slou>GFP* embryos labeled for GFP. Control and *bsd*^{1} embryos showed an equivalent number of GFP+ cells. (ns) not significant. Error bars represent SEM.

Figure S2, related to Figure 2. (A,B) Validation of the Bsd antibody. (A) Western blots of control (*w*^{1118}), *Df(2R)BSC199,* and *rp298>Bsd* embryo lysates using the Bsd antibody (left) or preimmune serum (right). UAS/Gal4 expressed Bsd was detectable, but we could not detect endogenous Bsd by Western blot. (B) Western blot of S2 cell lysates transfected with control or Bsd.Myc expressing plasmids. The Bsd and Myc antibodies recognized proteins of the same molecular weight. (D) Stage 12 embryos immunolabeled with the Bsd antibody (green) and Mef2 (violet). Signal from the Bsd antibody was not observed in *Df(2R)BSC199* myonuclei. The embryos shown here were prepared in parallel.

Figure S3, related to Figure 3. (A) Mononucleate LO1 myotubes from Stage 12 *slou>GFP* embryos labeled for γ-tubulin (green), GFP (violet) and DAPI (blue). Control (*bsd*^{1}*/Cyo*) myotubes showed only cortical γ-tubulin foci. *bsd*^{1} myotubes had an equivalent number of cortical γ-tubulin foci compared to controls. (B) Quantification of γ-tubulin foci in multinucleate Stage 12 myotubes. Embryos used for (A,B) were derived from the same preparation. (ns) not significant. Error bars represent SEM.

Figure S4, related to Figure 4. (A) Coomassie stained control gel for GST immunoprecipitation experiment described in Figure 3. Bsd-bound GST beads (lane 5) recovered a large number of unique bands compared to control GST beads (lane 4). (B) Co-immunoprecipitation screen. S2 cells were transfected with Bsd.Myc and either a control plasmid (lane 2) or a plasmid expressing a Flag-tagged 'prey' protein (lanes 3-8) identified by AP-MS. Polo showed the strongest interaction with Bsd among the proteins tested. Lane 1 is a positive control. (C) Muscle morphogenesis phenotypes in *polo* mutants. Stage 16 embryos labeled with Tropomyosin. DT1, LO1, and VL1 muscles are pseudocolored orange, green, and violet. The polo alleles showed stronger phenotypes showed stronger phenotypes in trans to *Df(3L)BSC447* that uncovers *polo*, arguing the alleles are hypomorphic. Quantification of muscle phenotypes is as described in Fig. 1.

Figure S5, related to Figure 5. (A) Control phosphorylation assay. Lysates from S2 cells transfected with a control plasmid or a plasmid expressing Bsd.Myc were immunoblotted with anti-phospho-threonine (pThr). Whole lystates showed equivalent pThr levels. (B) *in vitro* phosphorylation assay. Polo was immunoprecipitated from S2 cell lysates and blotted with a phospho-threonine (pThr) antibody. Cells transfected with Bsd.I129A showed equivalent phosphorylated Polo as controls. (C) Stage 12 embryos with an endogenous GFP-tagged Polo ($Polo^{GFP}$) that expressed *rp298>nLacZ* were immunolabeled for GFP (green) and lacZ (red). Localization of total Polo protein was comparable between control and bsd^1 embryos. Graph shows Polo and nlacZ fluorescent intensity across myoblasts. (D) Early and late Stage 12 embryos immunolabeled for phospo-Polo (pPolo, green) and Mef2 (violet). pPolo localization in myonuclei increased during Stage 12 in control (bsd^1 heterozygous) but not bsd^1 embryos. Control and bsd^1 embryos were labeled in the same preparation. (E) Immunoprecipitation of S2 cell lysates transfected with Bsd and Pav. Bsd did not physically interact with Pav.

Figure S6, related to Figure 6. (A) C2C12 cells treated with control (scrambled) siRNA or a cocktail of two siRNAs against murine Vrk1, Vrk2, or Vrk3. Cells were fixed after 7 days in differentiation media and labeled for α-actinin (green) to detect differentiated myotubes, F-actin (violet) and DAPI (blue). Vrk3 knockdown myotubes were shorter than controls and often rounded. Vrk1 and Vrk2 knockdown myotubes were indistinguishable from control cells. (B) Quantitative real time PCR of siRNA treated C2C12 cells. Fold change is relative to control

treated cells (red line). (C) QQ plot of myotube distribution, related to figure 6C. **($p<0.01$), ****($p<0.0001$). Error bars represent SEM.

Figure 1. The ser/thr kinase Bsd regulates muscle morphogenesis

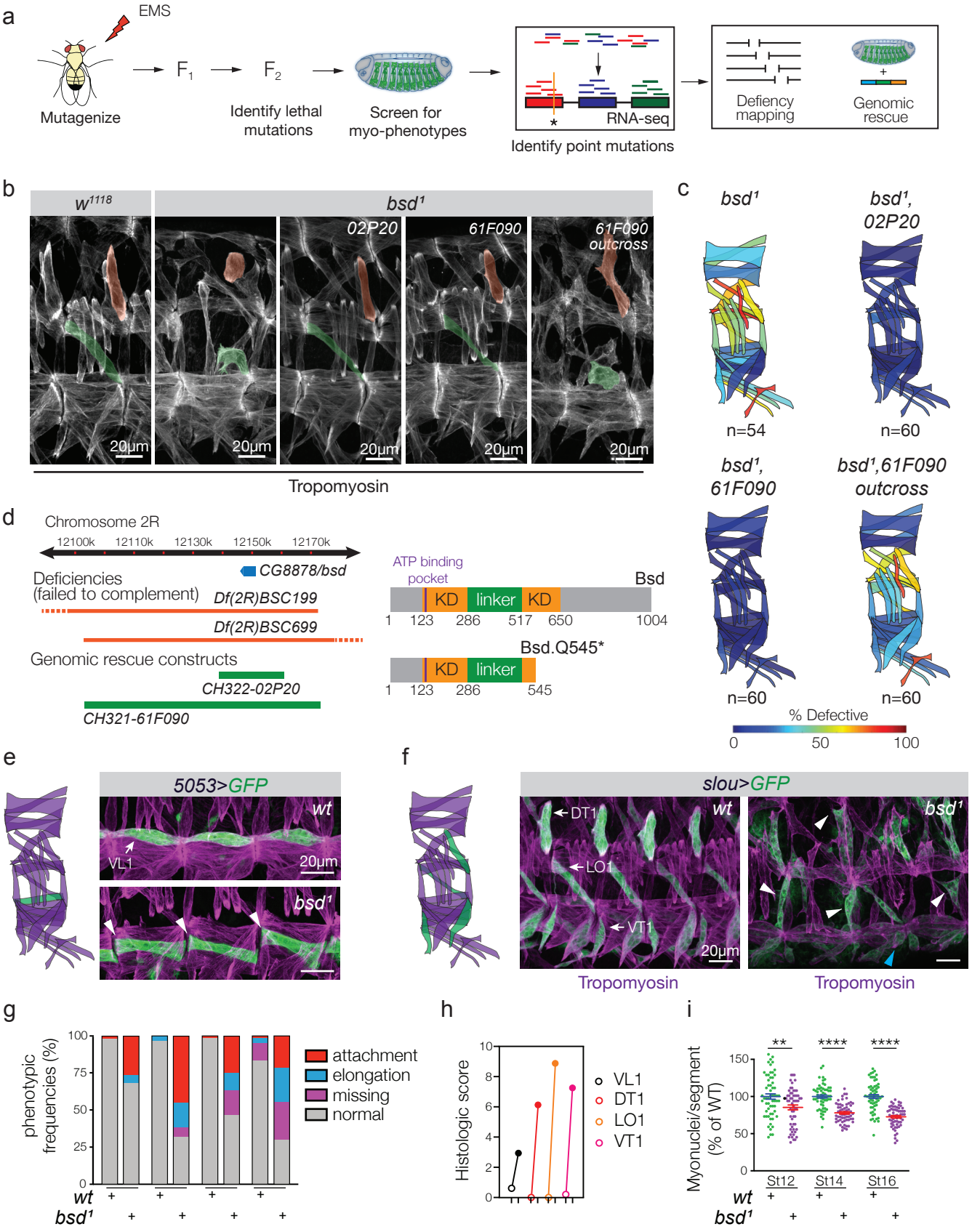

Figure 2. Bsd kinase activity in the mesoderm directs myotube guidance and Bsd protein localization is dynamic

a

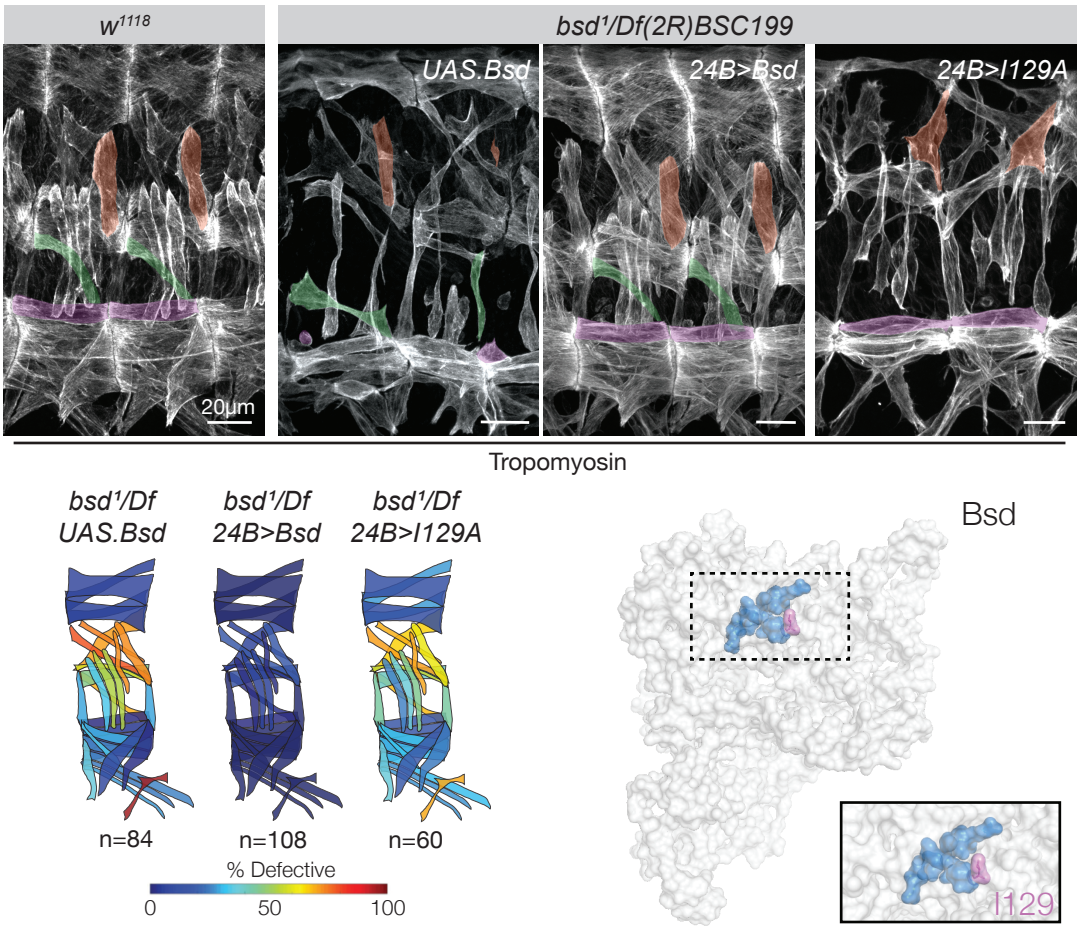

b

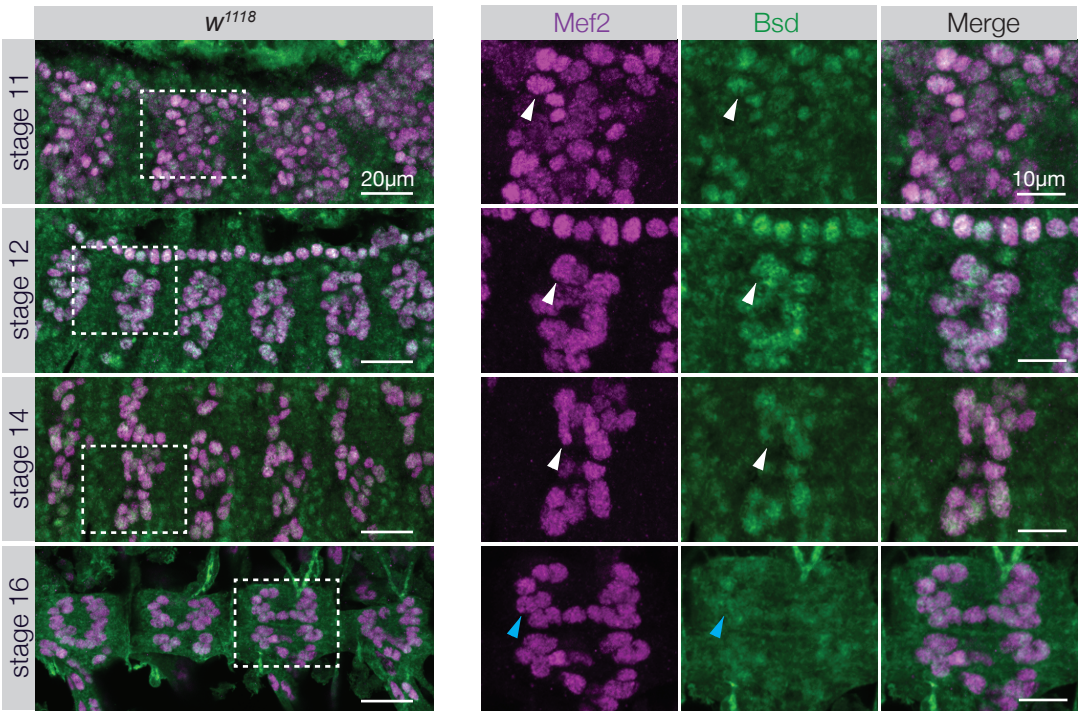

Figure 3. Microtubule reorganization during myotube guidance requires Bsd

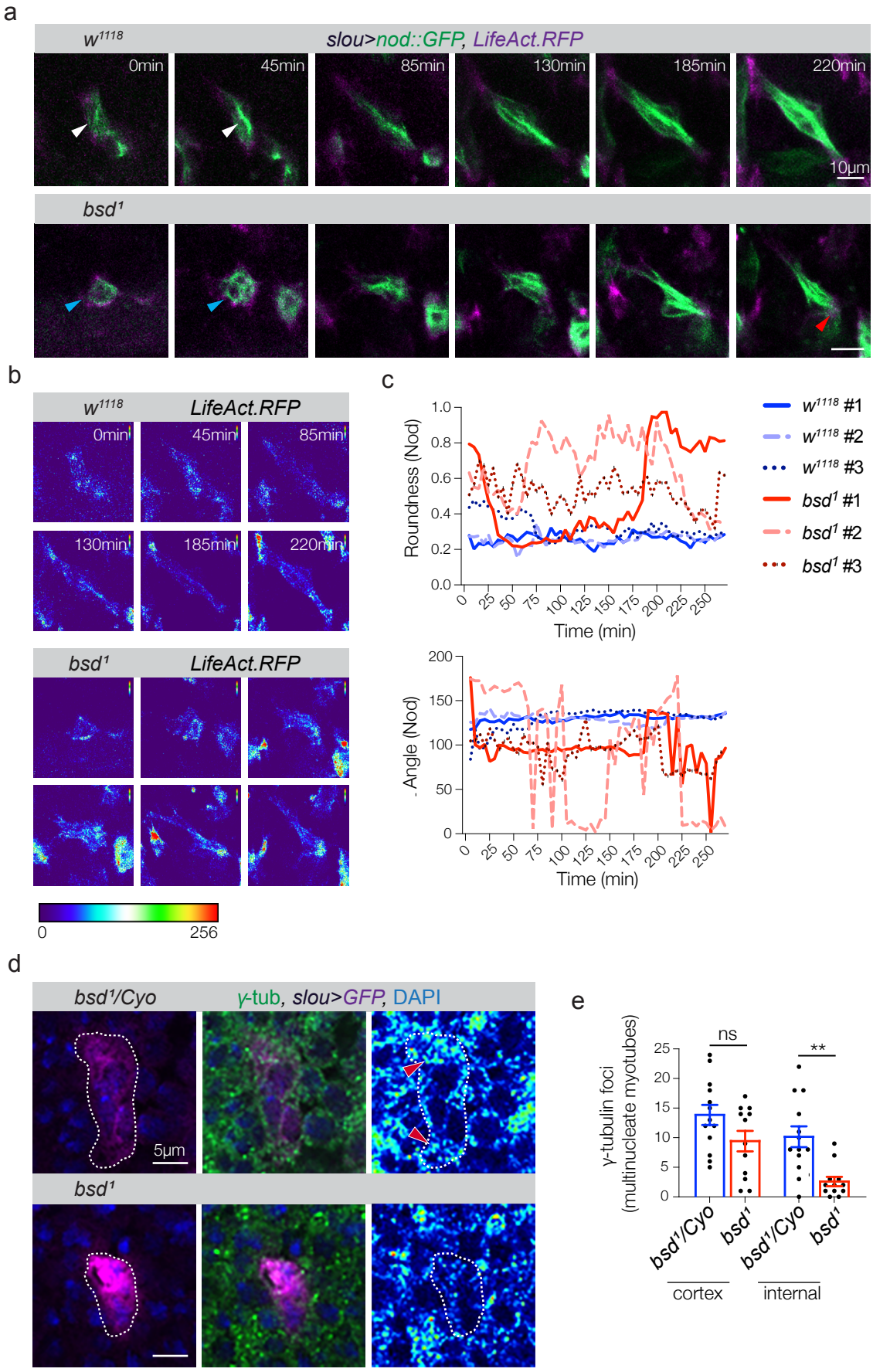

Figure 4. Bsd and Polo kinase are in a common myogenic pathway

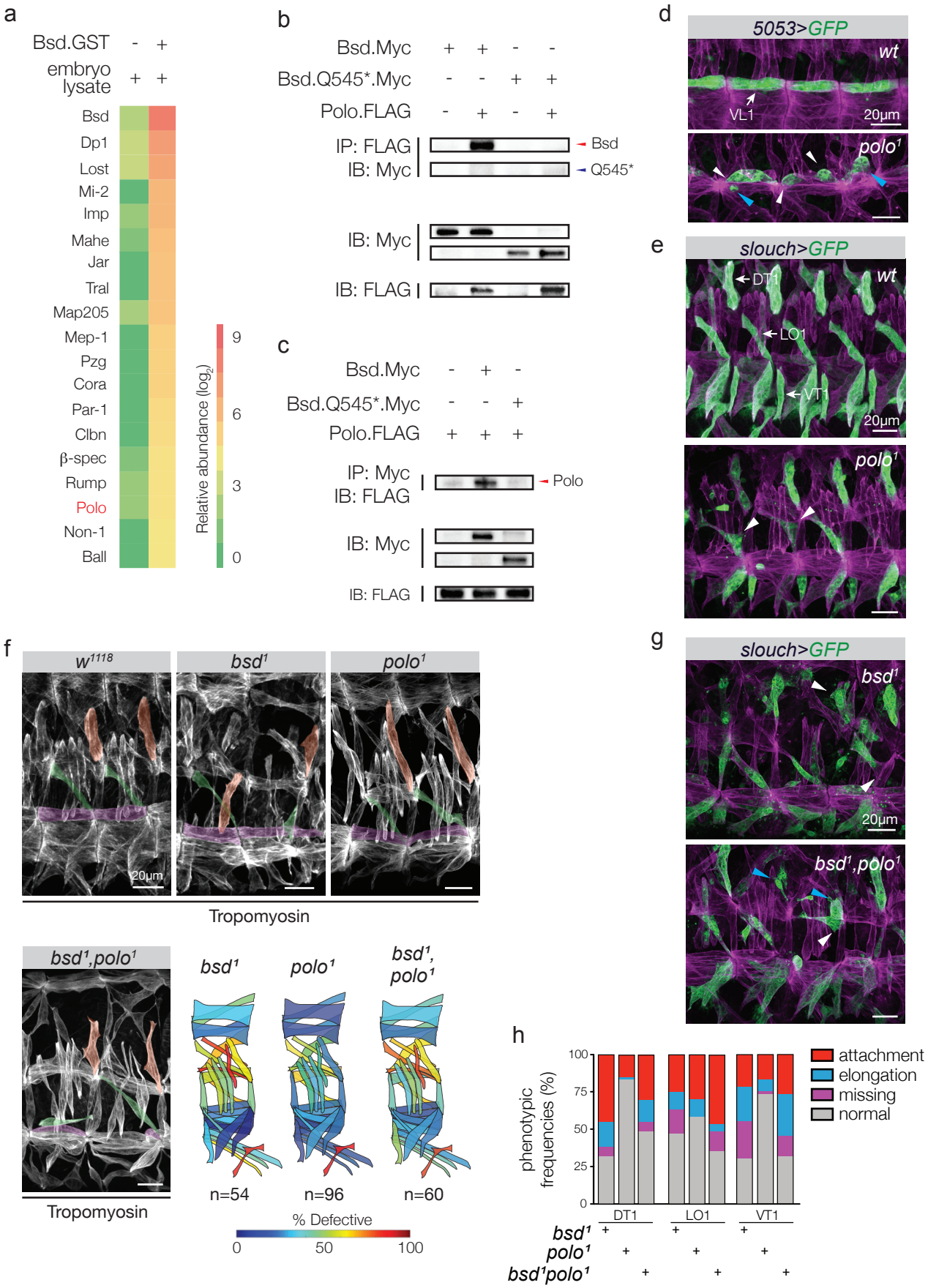

Figure 5. Bsd activates Polo to direct myotube guidance

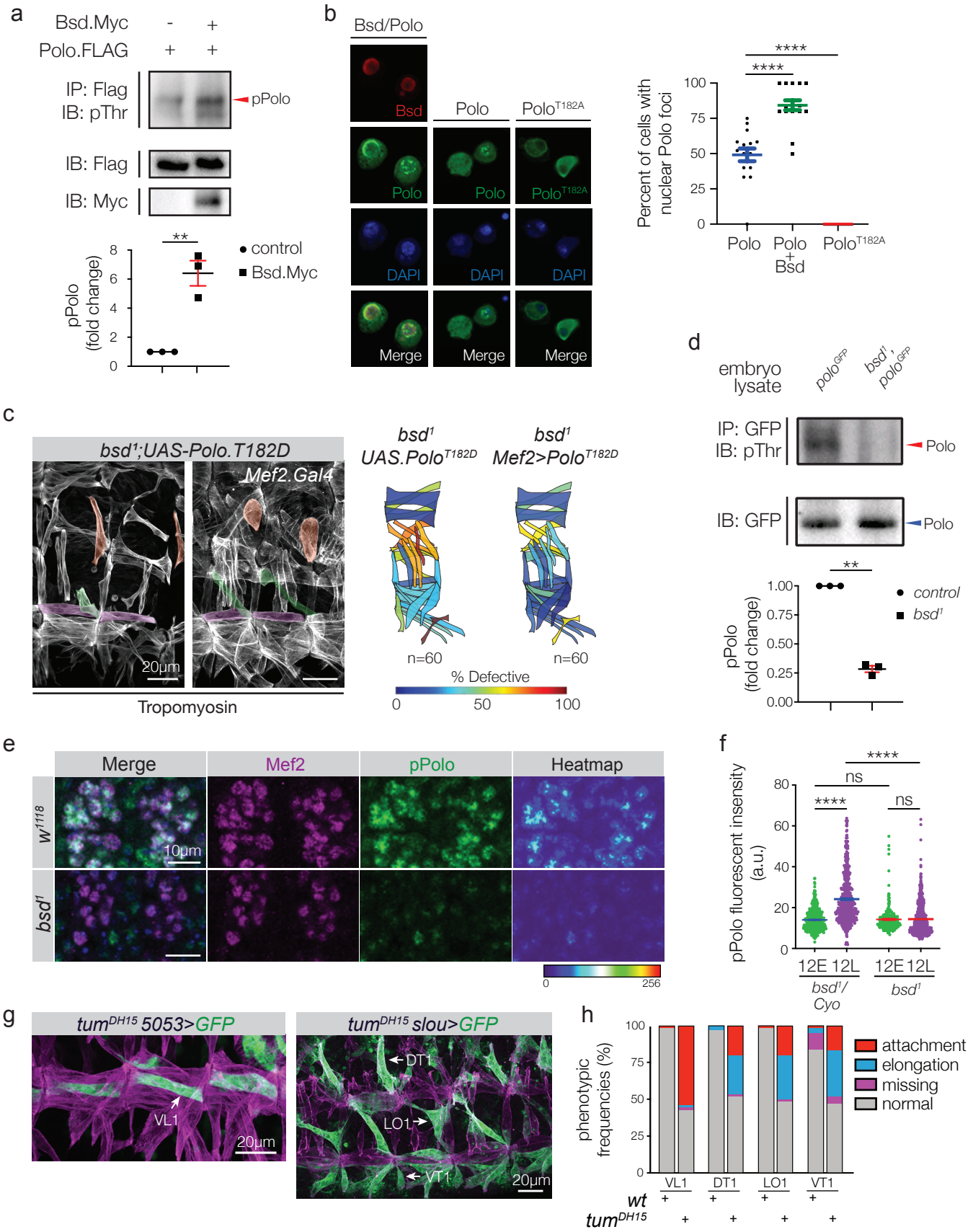

Figure 6. The Bsd orthologue Vrk3 is required for myotube elongation

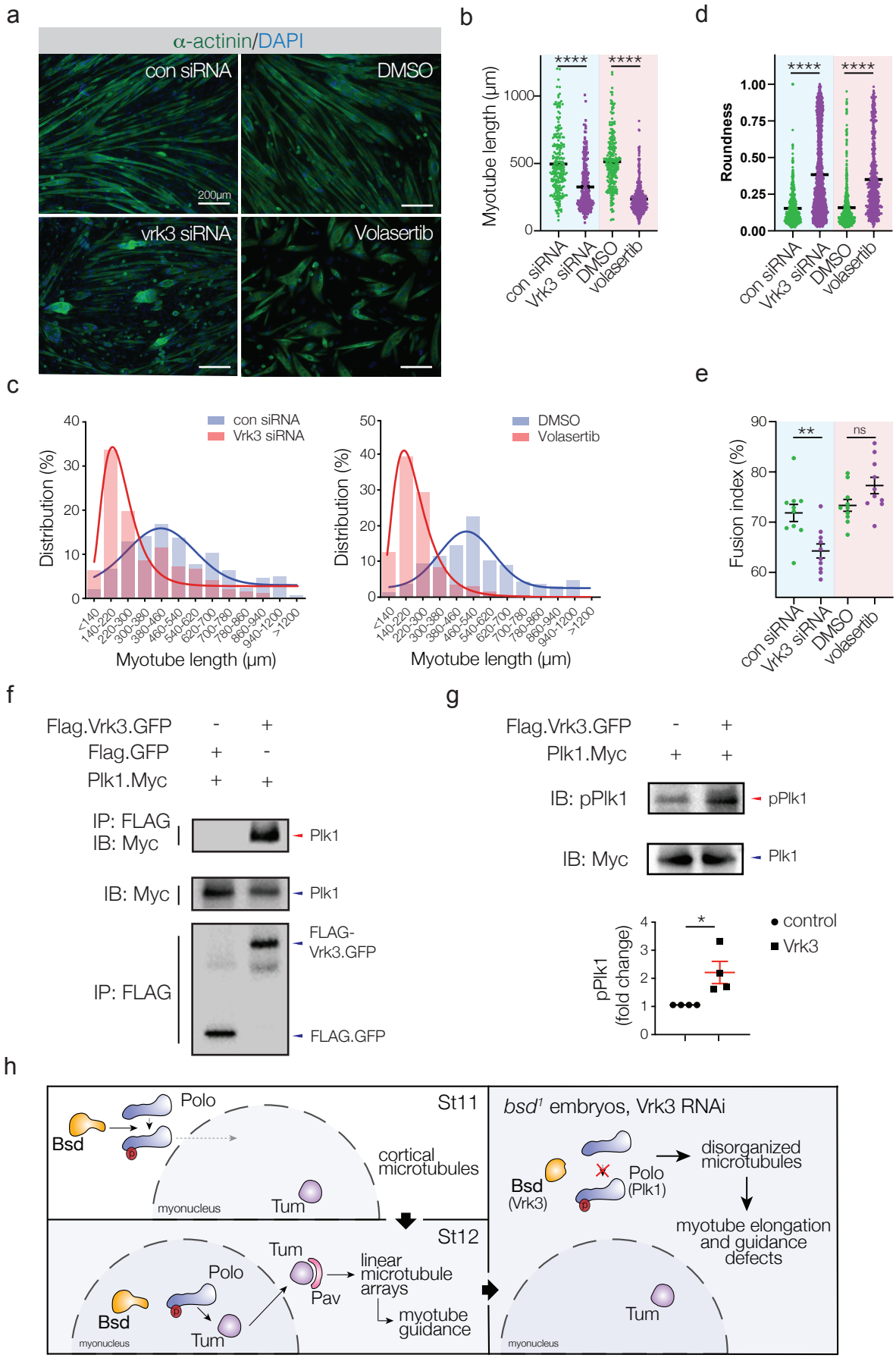

Figure S1, related to Figure 1

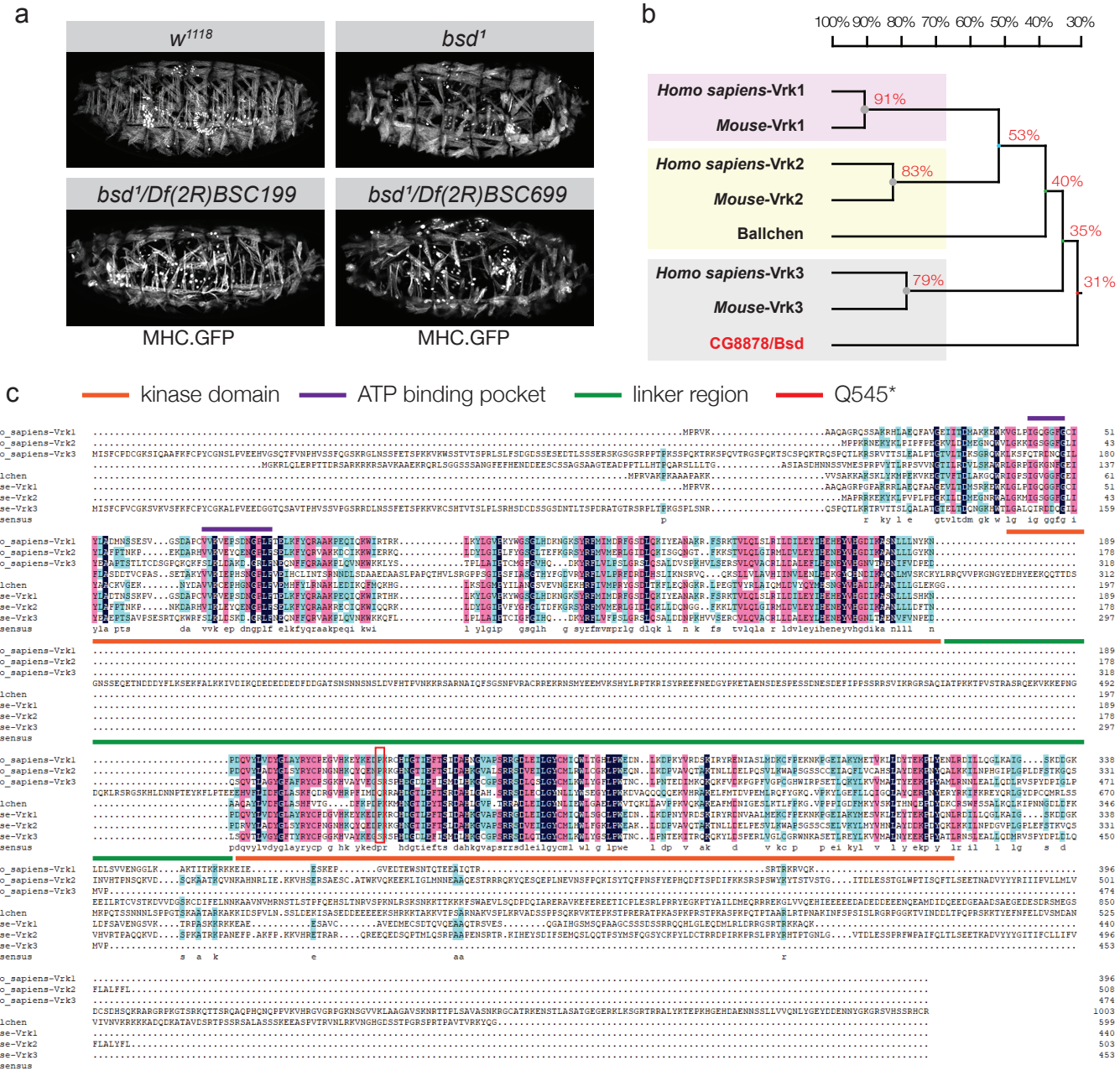

Figure S2, related to Figure 2

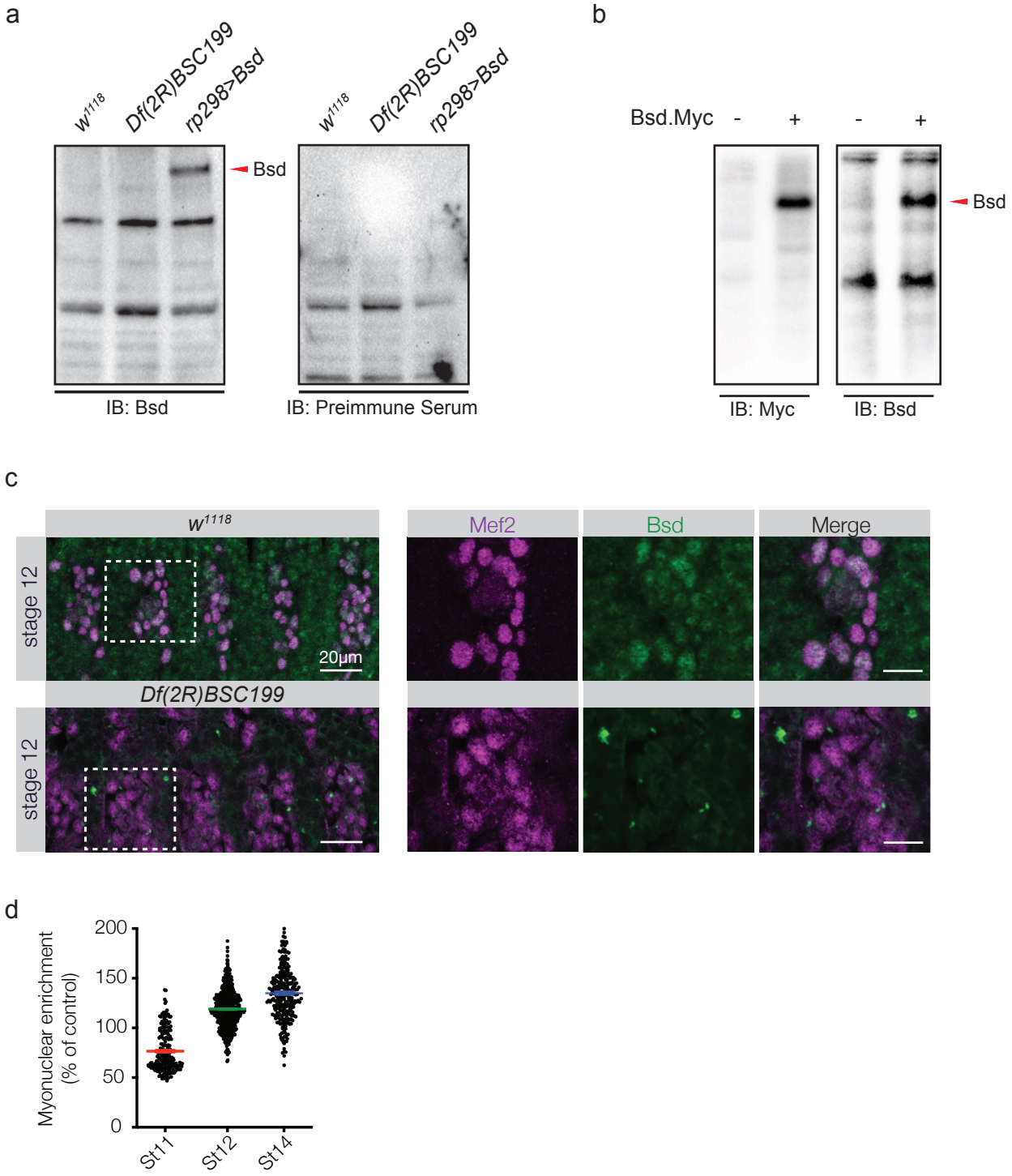

Figure S3, related to Figure 3

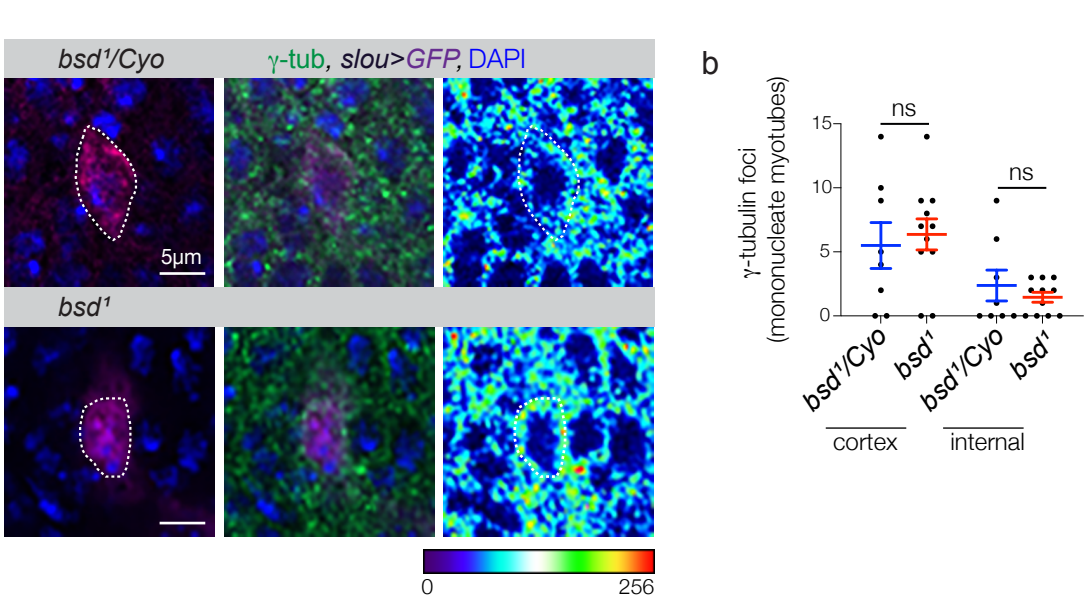

Figure S4, related to Figure 4

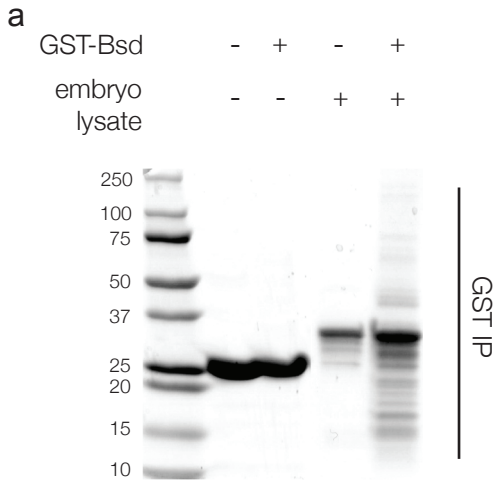

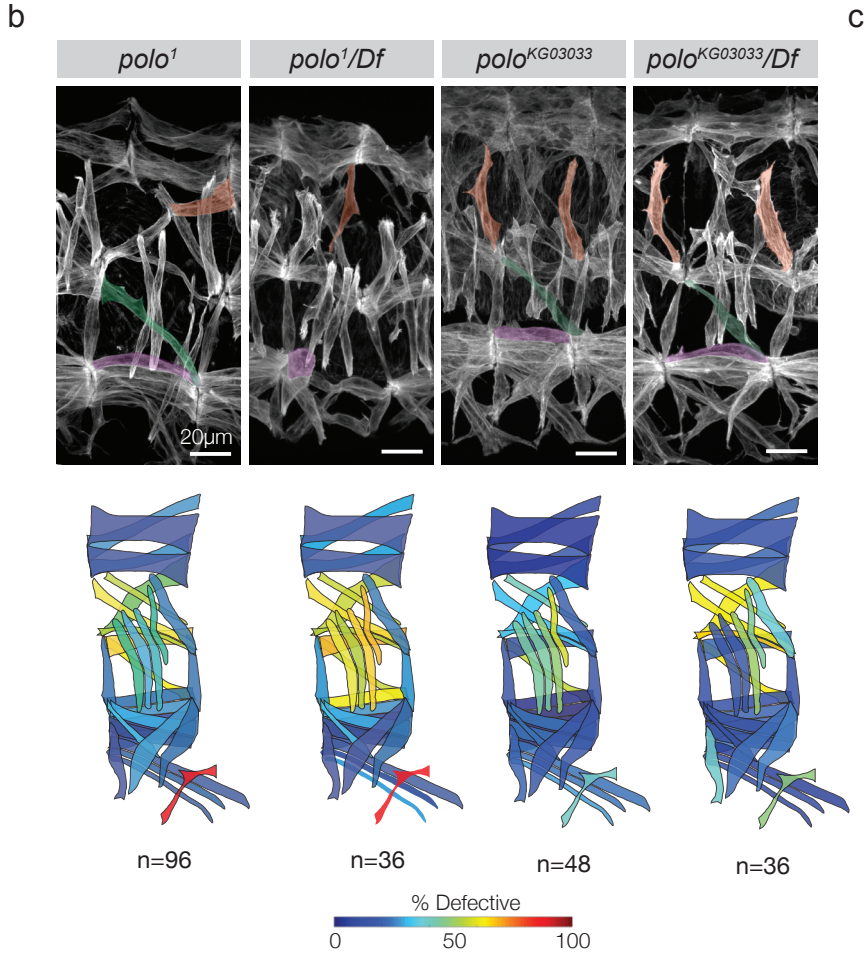

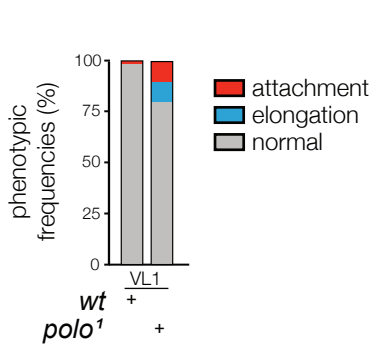

Figure S5, related to Figure 5

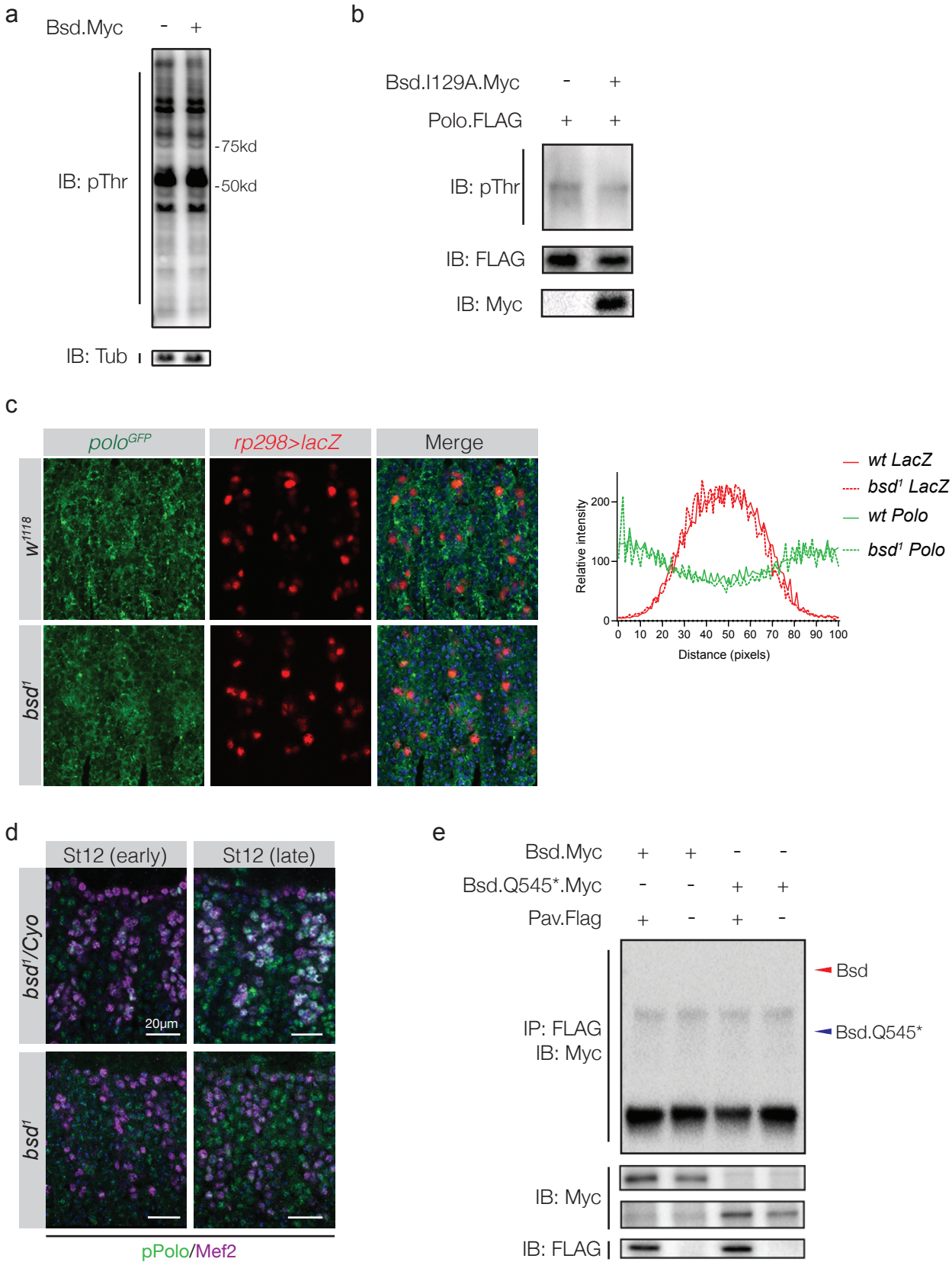

Figure S6. Related to Figure 6

a

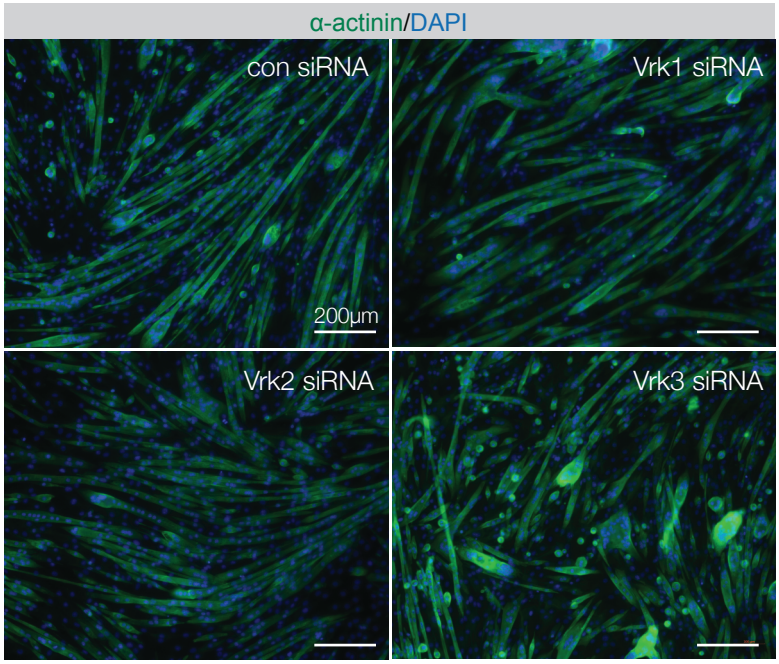

b

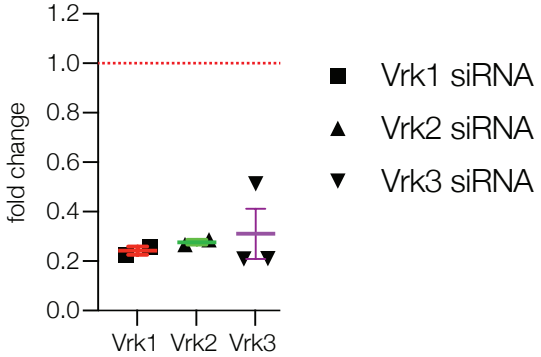
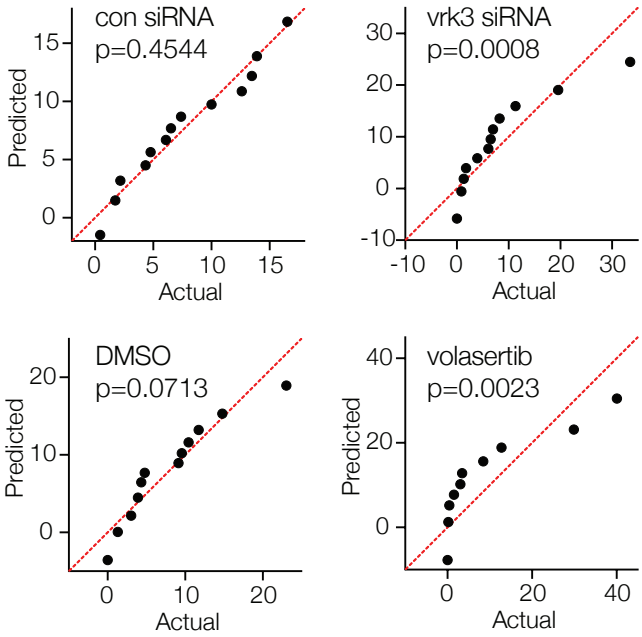
c